Raindrop Size Distribution and Rain Characteristics during the 2013 Great Colorado Flood

KATJA FRIEDRICH, EVAN A. KALINA, AND JOSHUA AIKINS

Department of Atmospheric and Oceanic Sciences, University of Colorado Boulder, Boulder, Colorado

MATTHIAS STEINER, DAVID GOCHIS, PAUL A. KUCERA, KYOKO IKEDA, AND JUANZHEN SUN

National Center for Atmospheric Research, Boulder, Colorado

(Manuscript received 20 September 2014, in final form 16 March 2015)

ABSTRACT

Drop size distributions observed by four Particle Size Velocity (PARSIVEL) disdrometers during the 2013 Great Colorado Flood are used to diagnose rain characteristics during intensive rainfall episodes. The analysis focuses on 30 h of intense rainfall in the vicinity of Boulder, Colorado, from 2200 UTC 11 September to 0400 UTC 13 September 2013. Rainfall rates R, median volume diameters D_0 , reflectivity Z, drop size distributions (DSDs), and gamma DSD parameters were derived and compared between the foothills and adjacent plains locations. Rainfall throughout the entire event was characterized by a large number of small- to medium-sized raindrops (diameters smaller than 1.5 mm) resulting in small values of $Z (<40 \,\mathrm{dB}Z)$, differential reflectivity $Z_{\rm dr}$ (<1.3 dB), specific differential phase $K_{\rm dp}$ (<1° km⁻¹), and D_0 (<1 mm). In addition, high liquid water content was present throughout the entire event. Raindrops observed in the plains were generally larger than those in the foothills. DSDs observed in the foothills were characterized by a large concentration of small-sized drops (d < 1 mm). Heavy rainfall rates with slightly larger drops were observed during the first intense rainfall episode (0000-0800 UTC 12 September) and were associated with areas of enhanced low-level convergence and vertical velocity according to the wind fields derived from the Variational Doppler Radar Analysis System. The disdrometer-derived Z-R relationships reflect how unusual the DSDs were during the 2013 Great Colorado Flood. As a result, Z-R relations commonly used by the operational NEXRAD strongly underestimated rainfall rates by up to 43%.

1. Introduction

Extreme events such as the 2013 Great Colorado Flood are difficult to forecast since their weather patterns and atmospheric processes do not resemble the standard conditions of a region for which forecasting and now-casting systems may have been tuned. Nevertheless, evaluating model performance and analyzing the interaction between dynamical and microphysical processes provides interesting insights, which might be applicable to other regions. The Great Colorado Flood was triggered by an atypical weather pattern that transported large amounts of warm and moist air over several days between 11 and 15 September from the Gulf of Mexico, the Caribbean Sea, and the tropical eastern

Corresponding author address: Dr. Katja Friedrich, Dept. of Atmospheric and Oceanic Sciences, University of Colorado Boulder, UCB 311, Boulder, CO 80309. E-mail: katja.friedrich@colorado.edu

DOI: 10.1175/JHM-D-14-0184.1

Pacific Ocean into the Front Range of northern Colorado. A detailed overview of the meteorological and hydrological conditions during the Great Colorado Flood and an evaluation of several quantitative precipitation estimates, quantitative precipitation forecasts, and hydrological forecast products can be found in Gochis et al. (2015).

Friedrich et al. (2015) analyzed the spatial and vertical structure of clouds and precipitation during the intensive rainfall episodes between 2200 UTC 11 September and 0400 UTC 13 September 2013 using radar reflectivity from the operational NEXRAD at Denver, Colorado (also referred to as KFTG). That study shows that the strongest rainfall occurred along the lower parts of the Colorado Front Range at ~1.6 km MSL. Friedrich et al. (2015) also concluded that rainfall type and distribution are strongly linked to mesoscale upslope strength in addition to smaller-scale and short-lived low-level convergence that resulted from the interaction with the local terrain (e.g., cyclonic circulation in the early hours of

12 September, also referred to as mesovortex; Friedrich et al. 2015; Gochis et al. 2015; Morales et al. 2015). The generating mechanisms of the low-level convergence and mesovortex are still being investigated, but first results hint toward the role of latent heat release and the influence of local topography (Morales et al. 2015). These smaller-scale and short-lived periods of convergence and the mesovortex, and their interaction with the local terrain, in conjunction with the larger-scale, persistent upslope flow, have been identified as the main driving mechanisms for the distribution, amount, and vertical structure of clouds and rain during the 2013 Great Colorado Flood. Mesoscale surface features directed the moisture to very localized areas, triggering convective and enhancing orographic precipitation over many hours that resulted in the devastating floods. The mesovortex, a mesoscale, counterclockwise circulation that developed over Denver in the late evening on 11 September, was one of those notable features. In the early hours of 12 September, this circulation, accompanied by several bands of enhanced surface convergence, moved northwestward toward the Boulder, Colorado, area and farther up the mountains. During weak low-level forcing, rain at and below the melting layer was produced through collision-coalescence processes. During stronger lowlevel forcing, higher cloud tops with layers of supercooled liquid favored graupel production. During this time, lightning was observed along the Front Range between 0330 and 0634 UTC 12 September [Fig. 13 in Friedrich et al. (2015)]. Eight hours of intense rainfall between 0000 and 0800 UTC 12 September (hereafter also referred to as the first episode) was observed in the foothills between Golden and Estes Park, mainly as a result of the convergence bands and their interaction with the local terrain. On the evening of 12 September, low-level easterly flow persisted for over 8 h and resulted in a second episode of intense rainfall mainly over the foothills between 2000 UTC 12 September and 0400 UTC 13 September (hereafter also referred to as the second episode). No lightning was observed during the second episode.

Friedrich et al. (2015) and Gochis et al. (2015) focus on the meteorological and hydrological setup and the temporal and spatial distribution of rainfall on a larger spatial scale. In contrast, the present study analyzes the spatial and temporal evolution of drop size distributions (DSDs) and rain characteristics (intensity, mean diameter, and number concentration) measured by optical disdrometers at four locations along the Colorado Front Range during the intensive rainfall episodes. DSDs observed during the first and second intense rainfall episodes are compared and analyzed with respect to the low-level convergence field and the microphysical processes. In addition, DSDs from two lower-elevation

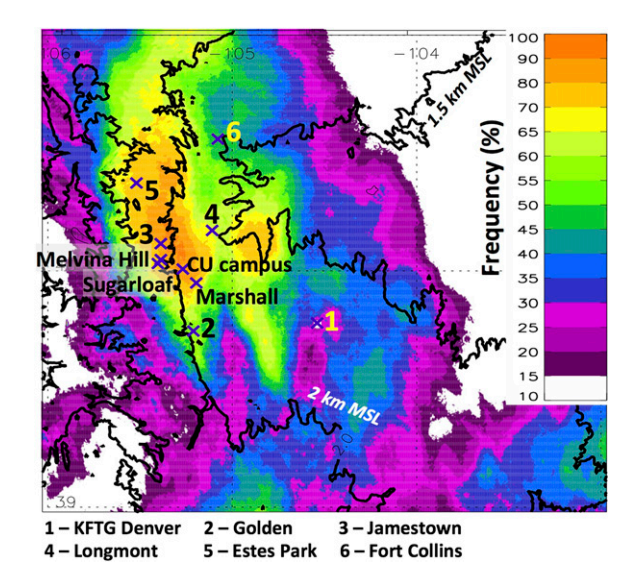


FIG. 1. Relative frequency of $Z > 15\,\mathrm{dB}Z$ observed at each radar range gate from the surface to $500\,\mathrm{m}$ AGL between $2200\,\mathrm{UTC}$ 11 Sep and $0400\,\mathrm{UTC}$ 13 Sep. Reflectivity was observed every 5 min by the operational WSR-88D at Denver resulting in a total of 360 radar scans (100%). Black lines denote terrain height contours at 1.5, 2, 3, and 4 km MSL. Crosses with numbers indicate the approximate town and city center locations (names of cities are shown below) and instrument locations at Marshall, CU campus, Melvina Hill, and Sugarloaf.

stations on the plains are compared to two stations in the foothills to investigate the effects of the local terrain on the rainfall characteristics.

2. Instruments and methods

a. Disdrometers

A total of four OTT Particle Size and Velocity (PARSIVEL; Löffler-Mang and Joss 2000; Tokay et al. 2014) optical disdrometers collected data during the Great Colorado Flood, with their locations shown in Fig. 1. Two first-generation OTT PARSIVELs were located at the University of Colorado (CU) campus in Boulder (1663 m MSL; hereafter referred to as CU campus) and at the National Center for Atmospheric Research (NCAR) facility at Marshall ~5 km south of CU campus (1742 m MSL; hereafter referred to as Marshall; Rasmussen et al. 2012), respectively. Two first-generation PARSIVEL disdrometers operated by NCAR were deployed within the Fourmile Canyon ~5 km west of CU campus close to Sugarloaf Mountain (2225 m MSL; hereafter referred to as Sugarloaf) and Melvina Hill (2431 m MSL). Observations were conducted continuously at Sugarloaf, CU campus, and Marshall. Because of a power failure, the disdrometer at Melvina Hill only operated from 2300 UTC 11 September to 0800 UTC 12 September and at 1800-1900 and 2100-2330 UTC 12 September 2013.

The PARSIVEL disdrometers use a 650-nm laser with a power of 3 MW (Löffler-Mang and Joss 2000; Löffler-Mang and Blahak 2001). The laser produces a horizontal sheet of light 30 mm wide and 180 mm long, resulting in a horizontal sampling area of 54 cm². Particles passing through the horizontal sampling area cause a reduction of the light intensity that is proportional to the particle size. The particle velocity is estimated from the duration of the reduction in light intensity and the particle size from the magnitude of the reduction, with the assumption that the particles are spherical [Fig. 1 in Löffler-Mang and Joss (2000)]. The particle size and fall velocity of each particle are sorted into 32 velocity classes ranging between 0.05 and 20 m s⁻¹ and 32 particle size classes ranging between 0.062 and 24.5 mm. Because of the small signal-to-noise ratio, no particles are recorded in the smallest two size classes, resulting in a minimum detectable size of about 0.312 mm. The class width is finer for smaller- and medium-sized particles and broadens for larger particles [see Fig. 1 and Table A1 in Yuter et al. (2006)]. During the 2013 Great Colorado Flood, the four disdrometers operated with different temporal sampling intervals: CU campus sampled at 30 s, Marshall at 1 min, and Sugarloaf and Melvina Hill at 5 min. A detailed description and specification of the instrument's hardware and data analysis are found in Löffler-Mang and Joss (2000), Löffler-Mang and Blahak (2001), Yuter et al. (2006), Friedrich et al. (2013a,b), and Tokay et al. (2014, and references therein). Differences in uncertainty relevant for this study are discussed in the appendix.

b. Methods for disdrometer analysis

Various error sources have been identified that affect the quality of the PARSIVEL disdrometer observations, for example, instrument background noise, large uncertainties for rainfall rates >20 mm h⁻¹, mixed-phase precipitation, strong winds and turbulence, margin fallers, and splashing of raindrops on the instrument housing (e.g., Nešpor et al. 2000; Krajewski et al. 2006; Thurai et al. 2011; Jaffrain and Berne 2011; Tokay et al. 2013, 2014, and references therein). A quality-control procedure described in Friedrich et al. (2013a,b) was applied to the recorded particle size distributions, which removed margin fallers, splashing drops, and particles misclassified because of strong wind and heavy precipitation effects. The resulting number concentrations were used to calculate the moments of the DSD, including reflectivity Z, rainfall rate R, liquid water content W, median volume diameter D_0 , total number concentration N_T , and the generalized intercept parameter N_W at a temporal resolution of 1 min (CU campus and Marshall) and 5 min (Sugarloaf and Melvina Hill), as described in Friedrich et al. (2013b) and following Ulbrich (1983), Testud et al. (2001), Bringi et al. (2003), and Yuter et al. (2006).

After quality control, a global scaling analysis was conducted (see Sempere Torres 1994, 1998; Uijlenhoet et al. 2003) and a gamma function was fit to each raindrop size distribution following the method of moments (Tokay and Short 1996). The DSD function parameters [i.e., the shape μ (unitless), slope Λ (mm⁻¹), and intercept N_0 (mm^{-1- μ} m⁻³)] are derived from the third, fourth, and sixth moments of the DSD using Eqs. (3)–(5) in Tokay and Short (1996). In addition, the transition (T) matrix method (Vivekanandan et al. 1991; Bringi and Chandrasekar 2001) was used to compute differential reflectivity Z_{dr} for S-band (2.89 GHz) and specific differential phase K_{dp} for both S- and X-band (9.39 GHz) frequencies for each 60-s time step from the DSDs observed by the disdrometers. The drop shape model from Beard and Chuang (1987) was chosen. Note that only raindrops were observed at the disdrometer sites.

Rainfall rates and reflectivity calculated directly from the measured DSD were compared to rain gauge observations and measurements from the operational WSR-88D at Denver (i.e., KFTG), respectively (see the appendix). A detailed description of the KFTG radar operation during the Great Colorado Flood can be found in Friedrich et al. (2015). The rain gauges include a Geonor T-200B gauge at Marshall, an Environmental Technology Instruments (ETI) gauge at CU campus, and a tipping-bucket rain gauge at Melvina Hill [see, e.g., Rasmussen et al. (2012) for instrument type descriptions]. More information about the performance of the PARSIVEL disdrometer comparing the DSDs to a Joss-Waldvogel disdrometer (Joss and Waldvogel 1967) and rain gauges can be found in Tokay et al. (2013, 2014, and references therein).

c. Variational Doppler Radar Analysis System

Wind vector fields from the Variational Doppler Radar Analysis System (VDRAS; Sun and Crook 1997, 1998, 2001) were used to evaluate the dynamical forcing at lower versus higher elevations during the first and second intense rainfall episodes. VDRAS is a 4D variational data assimilation (4DVar) system that produces wind analyses using a mesoscale model background and observational data from radars and surface networks. In this study, the model background was provided by hourly forecasts generated by the Weather Research and Forecasting (WRF; Skamarock et al. 2005) Model run at a horizontal grid spacing of 3 km. Data from the operational observing networks were assimilated in VDRAS, including operational S-band polarimetric Doppler radar information from the radars at Denver, Colorado; Pueblo, Colorado; and Cheyenne, Wyoming; and NOAA's Meteorological Assimilation Data Ingest System (MADIS) surface

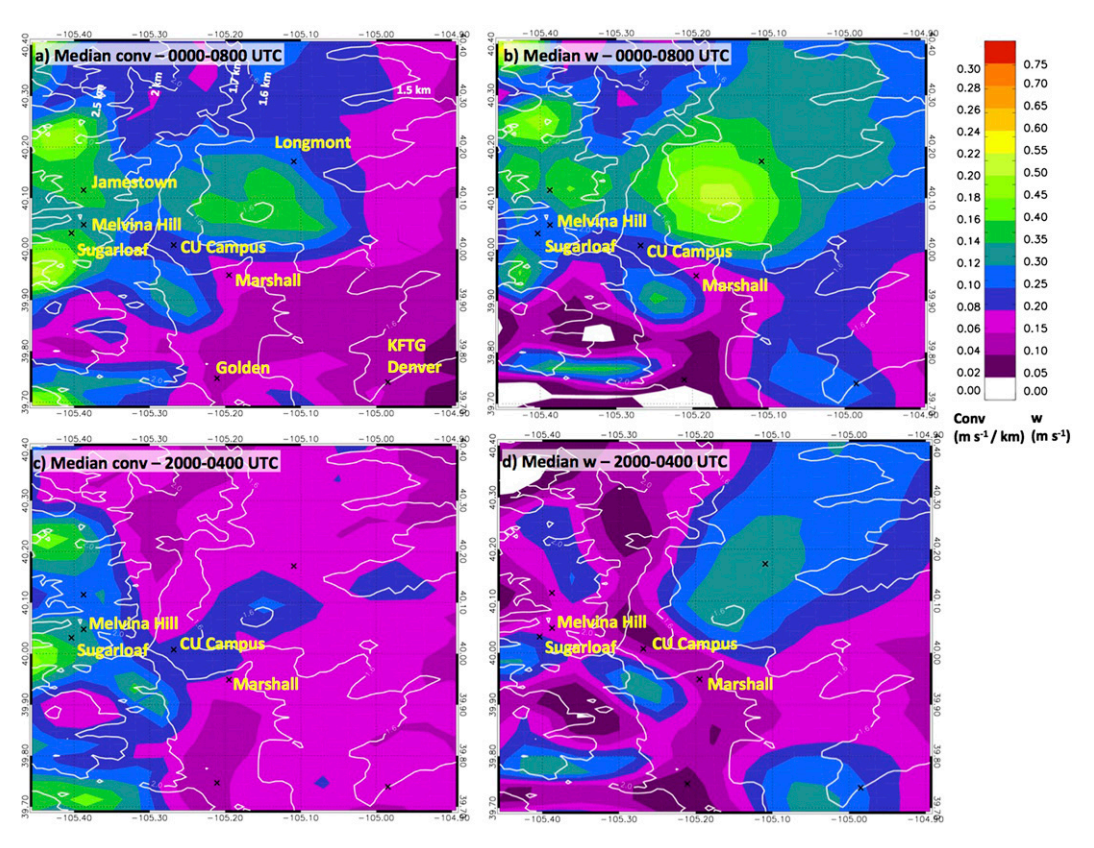


FIG. 2. Median (a),(c) convergence and (b),(d) vertical velocity from 2 to 8 km AGL based on VDRAS (top) between 0000 and 0800 UTC 12 Sep or (bottom) between 2000 UTC 12 Sep and 0400 UTC 13 Sep. White lines denote terrain height contours at 1.5, 1.6, 1.7, 1.8, 2, and 2.5 km MSL. Crosses approximate town and city center locations and instrument locations at Marshall, CU campus, Melvina Hill, and Sugarloaf.

observations (Sun and Crook 2001). The 4DVar was cycled every 10 min with a horizontal resolution of 3 km and a vertical resolution of 300 m, assimilating all available radar and surface observations within the 10 min assimilation window to produce an analysis valid at the end of that time window. The accuracy of VDRAS was verified against aircraft data (Sun and Crook 1998), profiler and surface data (Sun et al. 2010), and dual-Doppler synthesis (Crook and Sun 2002). The system has been used in operational settings in selected regions since 1998 (Sun and Crook 2001).

3. Spatial and temporal variability of rainfall characteristics

a. Spatial variation of rainfall and DSDs

The greatest and most persistent rainfall during the Great Colorado Flood was recorded during 11–13 September 2013 along the lower parts of the Colorado Front Range, as shown in the frequency analysis of intense rainfall in Fig. 1. As suggested in Friedrich et al. (2015)

using Doppler velocity fields, the rainfall distribution was strongly linked to low-level upslope flow interacting with the terrain. Fields of median convergence and vertical velocity derived from VDRAS in Fig. 2 show enhanced convergence and vertical velocity linked to the local terrain. Enhanced convergence and upward vertical motion occurred as the terrain height increased from 1.5 to 1.7 km MSL between CU campus and Longmont. At higher elevations (>2 km MSL), the strongest convergence and upward motion occurred from south of Sugarloaf to north of Jamestown (Fig. 2). During the first intense rainfall episode, strongest (weakest) median convergence was observed at Sugarloaf and Melvina Hill (Marshall), while CU campus experienced moderate median convergence and vertical velocity. However, the maximum convergence was observed at CU campus (figure not shown), where the greatest accumulated rainfall (113 mm; Table 1) was also observed. The weakest maximum convergence was observed at Marshall, which only recorded ~40 mm of accumulated rainfall during the first episode (Table 1). During the second episode, median convergence and

TABLE 1. Rainfall characteristics at the four disdrometer locations during the first and second intensive rainfall episodes; time of occurrence, number of 5-min samples, accumulated

		n 		
	Melvina Hill	Mean rai rate (mm h	7.3	5.4
rainfall, and mean rainfall rates.		No. of 5-min Accumulated Mean rain samples rain (mm) rate (mm h ⁻	83	17.8
		No. of 5-min samples	94	40
	Sugarloaf	No. of 5-min Accumulated Mean rain No. of 5-min Accumulated Mean rain (mm) rate (mm h ⁻¹) samples rain (mm) rate (mm h ⁻¹)	8.1	4
		Accumulated rain (mm)	61.6	32.3
		No. of 5-min samples	84	96
rainfall, and me		Mean rain rate (mm h^{-1})	5.5	9.2
ra	Marshall	Accumulated rain (mm)	39.3	73.5
		No. of 5-min samples	06	96
		o. of 5-min Accumulated Mean rain No. of 5-mi samples rain (mm) rate (mm h^{-1}) samples	12 Sep 12.2	ГС 12–13 Sep 9
	CU campus	Accumulated rain (mm)	irst episode 0000–0800 UTC 12 Sep 93 112.8 12.2	econd episode 2000–0400 UTC 12–13 Sep 96 71.6 9
		No. of 5-min samples	First episode 0 93	Second episod 96

vertical velocity were only slightly greater at the higher-elevation stations compared to the lower-elevation stations. However, while Marshall and CU campus accumulated $\sim \! 70 \, \text{mm}$ during the second episode, accumulated rainfall at Sugarloaf was only 30 mm.

Large concentrations of small-sized raindrops were recorded throughout the event (Gochis et al. 2015). The abundance of small raindrops was characteristic of the DSDs observed at both the lower- and higher-elevation stations (e.g., CU campus vs Sugarloaf) as shown in Fig. 3. At Sugarloaf, large concentrations ($\sim 10^4 \text{ mm}^{-3} \text{ m}^{-1}$) of small-sized drops ($d < 1 \,\mathrm{mm}$) were observed, with smaller concentrations (up to $10^2 \,\mathrm{mm}^{-3}\,\mathrm{m}^{-1}$) of mediumsized drops ($d \sim 1-3$ mm). Raindrop diameters >3 mm were only recorded during a few time periods at Sugarloaf (0500-0700 UTC 12 September, denoted as 6 and 7 in Fig. 3b, and around 0300 UTC 13 September, denoted as number 12), resulting in significant increases in rainfall rate $(R > 40 \,\mathrm{mm}\,\mathrm{h}^{-1})$. The DSDs at CU campus showed similar characteristics, with a slightly smaller (larger) concentration of small (medium)-sized raindrops compared to Sugarloaf. Individual episodes of increased drop diameters and concentrations (denoted as 1–5 and 8– 11 in Fig. 3a) resulted in intense rainfall $(R > 40 \,\mathrm{mm}\,\mathrm{h}^{-1})$.

In general, the disdrometer-observed rainfall characteristics were unusual for precipitation in Colorado. These unusual characteristics include relatively small drops with median volume diameters mainly below 1.5 mm and W often exceeding $1 \,\mathrm{g \, kg^{-1}}$ (Figs. 4b,c). Based on the disdrometer data, the abundance of small raindrops led to small median reflectivity ($Z \sim 24$ -30 dBZ; Fig. 4a) and small median diameters ($D_0 \sim 0.86$ – 0.93 mm; Fig. 4b) over the entire event. Drop diameters and, as a result, radar reflectivity, were, on average, slightly larger at the lower-elevation sites CU campus and Marshall (0.92-0.93 mm) compared to the higherelevation sites Melvina Hill and Sugarloaf (0.86-0.88 mm). Despite the abundance of small raindrops, liquid water content and rainfall rates at CU campus, Marshall, and Sugarloaf peaked at 1.8 g kg⁻¹ and $70 \,\mathrm{mm}\,\mathrm{h}^{-1}$, respectively (Figs. 4c,d). Although the lowerand higher-elevation stations both observed large concentrations of small raindrops, the slightly higher concentration of medium-sized raindrops led to somewhat higher rainfall rates, accumulated total precipitation, reflectivity, and liquid water content at the lower-elevation stations (CU campus and Marshall) relative to the foothills stations Melvina Hill and Sugarloaf (Fig. 4). However, during individual periods (e.g., 0500– 0700 UTC 12 September at Sugarloaf and 0400-0700 UTC 12 September at Melvina Hill) rainfall rates and liquid water content reached values at the higher-elevation stations that are comparable to the values observed at CU

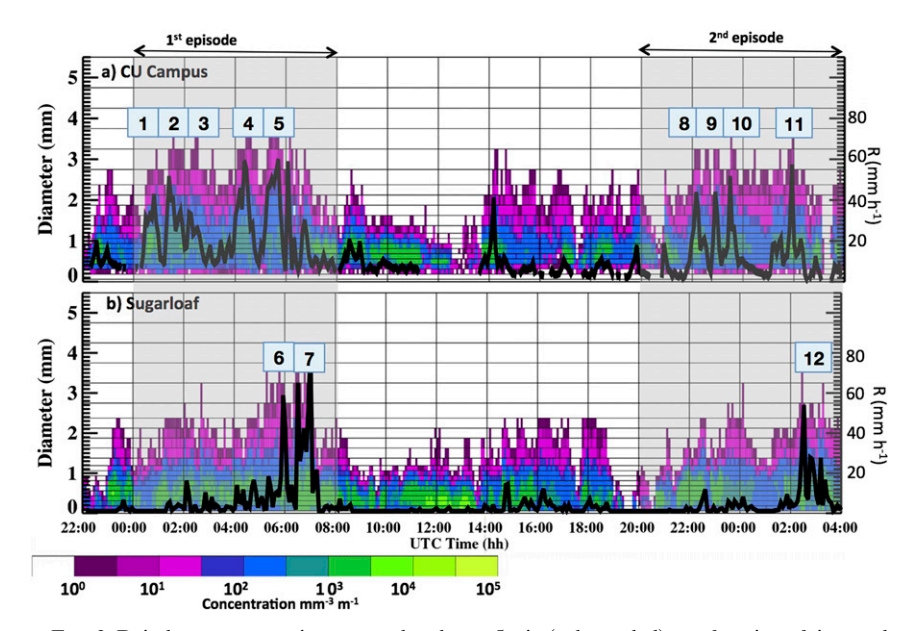


FIG. 3. Raindrop concentration accumulated over 5 min (color coded) as a function of time and diameter measured by the disdrometer at (a) CU campus and (b) Sugarloaf. Thick black lines represent rainfall rates based on 5-min DSD. Numbers indicate rainfall maxima discussed in the text. The first and second episodes of intense rainfall are indicated by gray-shaded background.

campus and Marshall. Median reflectivity, median liquid water content, and median rainfall rates at the lower-elevation stations (vs the foothills stations) ranged between 27.3 and 29.8 dBZ (23.9 and 25.3 dBZ), 0.17 and $0.23\,\mathrm{g\,kg^{-1}}$ (0.12 and $0.15\,\mathrm{g\,kg^{-1}}$), and 3.3 and 4.1 mm h⁻¹ (1.7 and 2.1 mm h⁻¹), respectively (Figs. 4a,c,d).

b. Temporal variation of rainfall and DSDs

While the patterns of enhanced convergence and vertical velocity were quite similar between the first and second episodes, convergence and vertical velocity differ greatly in magnitude (Fig. 2). Stronger convergence

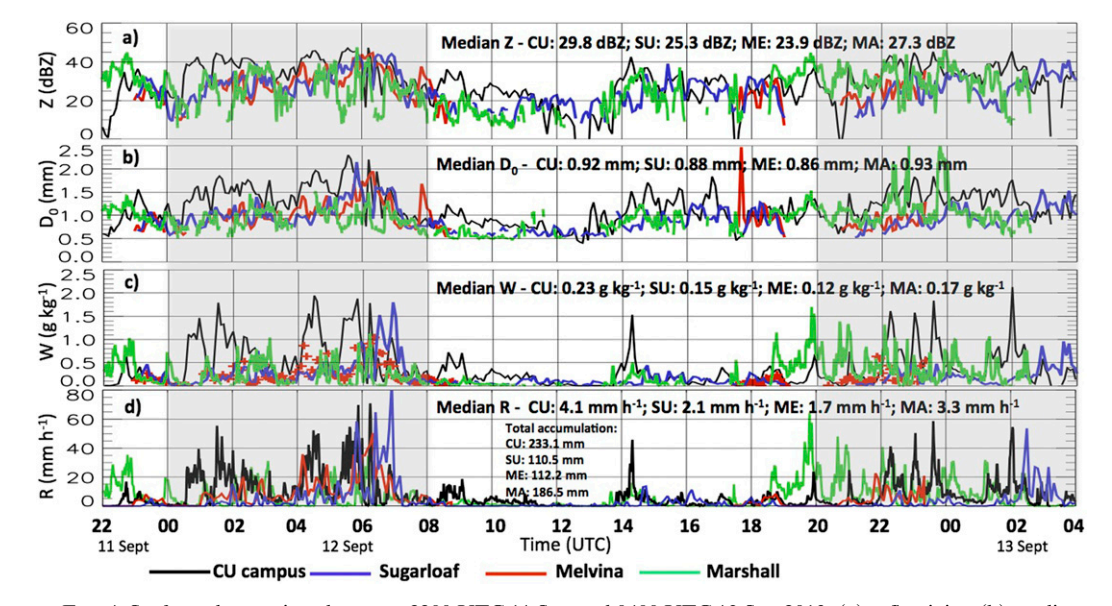


FIG. 4. Surface observations between 2200 UTC 11 Sep and 0400 UTC 13 Sep 2013: (a) reflectivity, (b) median volume diameter, (c) liquid water content, and (d) rainfall rate. Data are based on disdrometer observations at CU campus (CU; black lines), Sugarloaf (SU; blue lines), Melvina Hill (ME; red lines), and Marshall (MA; green lines). Median values calculated over the entire event at each station are indicated above. Total accumulated rainfall is given in (d). The first and second episodes of intense rainfall are indicated by a gray-shaded background. No rainfall measurements were available at Melvina Hill after 2300 UTC 12 Sep.

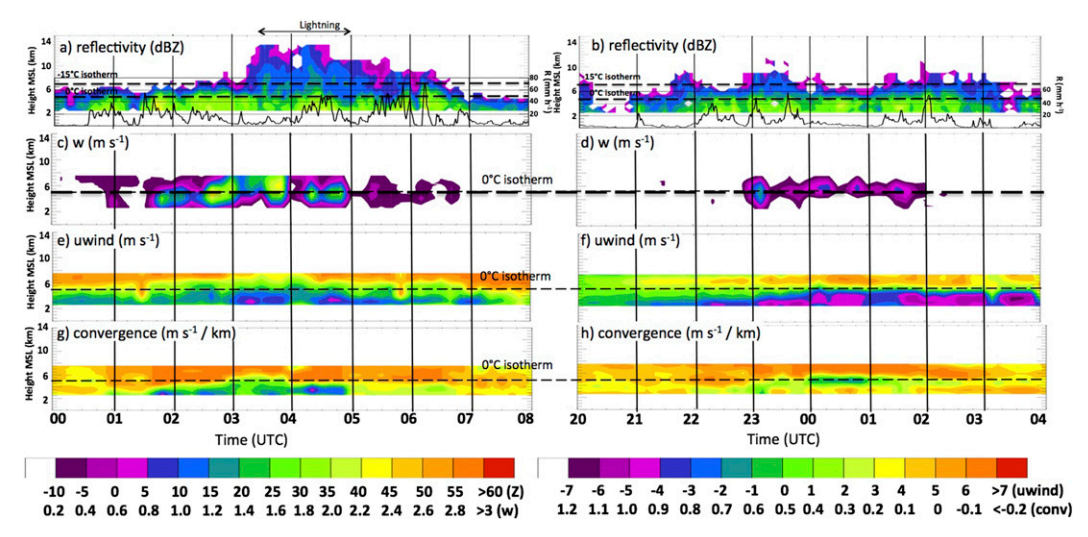


FIG. 5. Vertical profiles of (a),(b) reflectivity observed by the KFTG radar (color coded) and rainfall (solid black lines) observed by the disdrometer at CU campus and (c)–(h) parameters based on VDRAS at CU campus: (c),(d) vertical velocity; (e),(f) across barrier wind speed; and (g),(h) convergence for the (left) first and (right) second intensive rain episode. The time of lightning observations at CU campus are indicated in (a). Horizontal dashed lines indicate the 0° and -15° C isotherms.

and vertical velocity were observed during the first compared to the second episode together with larger accumulated rainfall and deeper clouds both at Sugarloaf and CU campus (Table 1; Figs. 2, 5, 6). Note that lightning was observed during the first episode, while no lightning occurred during the second episode. During the second episode, enhanced surface convergence >0.2 m s⁻¹ km⁻¹ only occurred occasionally (e.g., 2315, 2345, 0015, and 0130 UTC at CU campus in Fig. 5h), leading to a slightly enhanced updraft of >1 m s⁻¹ (Figs. 5d, 6d) that was much weaker compared to the first episode at CU campus and Sugarloaf.

Interestingly, stronger easterly surface flow was observed during the second compared to the first episode [Figs. 5e,f and 6e,f; see Fig. 9 in Friedrich et al. (2015)], which had no effect on the strength of the convergence. Enhanced low-level convergence of >0.3 m s⁻¹ km⁻¹ (<6 km MSL) was more persistent in time at Sugarloaf compared to CU campus. Since the dynamical forcing is different between the first and second intensive rain episodes and between the lower-and upper-elevation stations, the DSD analysis, presented in the following sections, will focus on these two time periods separately at CU campus and Sugarloaf.

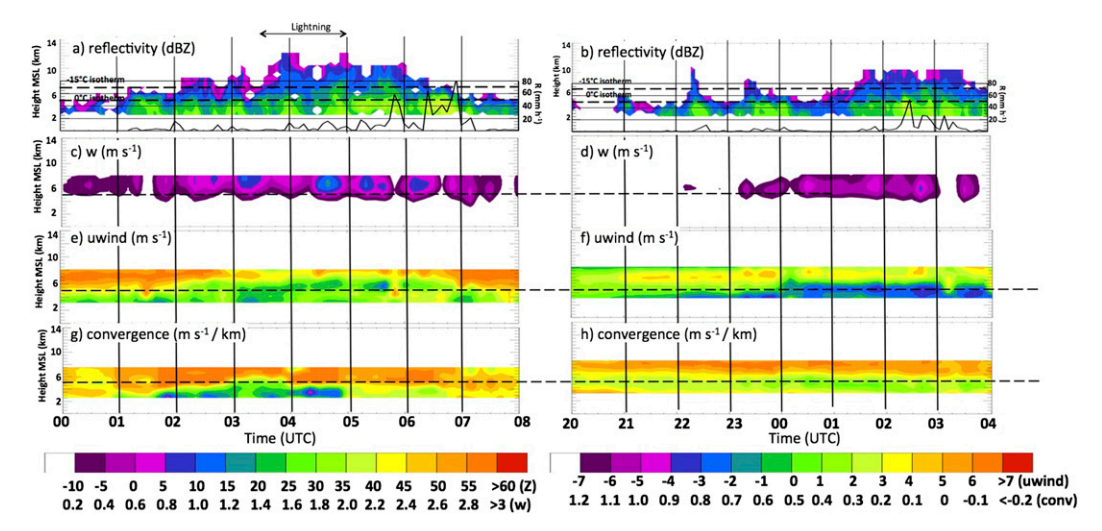


FIG. 6. As in Fig. 5, but for the Sugarloaf site.

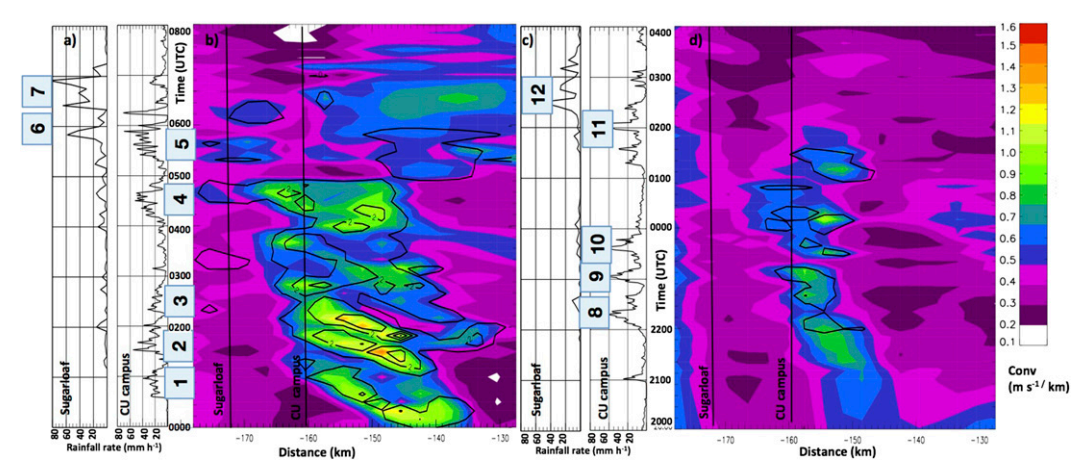


FIG. 7. (a),(c) Rainfall rate (solid black lines) as a function of time at Sugarloaf and CU campus and (b),(d) Hovmöller diagrams showing the max convergence (color coded) and max vertical velocity (solid black lines at 1, 2, and 3 m s⁻¹) from 2 to 8 km AGL (a),(b) at 0000–0800 UTC 12 Sep and (c),(d) between 2000 UTC 12 Sep and 0400 UTC 13 Sep. Numbers indicate rainfall maxima discussed in the text. The locations of Sugarloaf and CU campus are indicated as vertical black lines in (b) and (d).

Rainfall during the intense precipitation episodes was characterized by several bands of enhanced reflectivity or rainfall rates, which were more pronounced at CU campus than at Sugarloaf (Figs. 3, 4). Five rainfall maxima $(R > 40 \,\mathrm{mm}\,\mathrm{h}^{-1}; \mathrm{denoted})$ as 1–5 in Fig. 2) lasting up to 45 min were observed at CU campus. Sugarloaf also recorded two maxima with $R > 50 \,\mathrm{mm}\,\mathrm{h}^{-1}$ between 0600 and 0700 UTC (numbers 6 and 7 in Fig. 2). During the first episode, several convergence boundaries affected the distribution and intensity of the rainfall in the observational domain (Fig. 7a). Prior to 0600 UTC 12 September, the convergence boundaries formed 10-20 km upwind and reached the observational domain, but primarily remained in the lower foothills close to Boulder, as shown in the Hovmöller diagrams of maximum convergence in Fig. 7a. At higher-elevation stations, enhanced convergence ($>0.5 \,\mathrm{m\,s^{-1}\,km^{-1}}$) was not observed until 0430 UTC (Fig. 7a). Intense rainfall at CU campus and Sugarloaf correlate with the passage of areas of enhanced vertical velocity and convergence between 0000 and 0500 UTC. After 0500 UTC, intense rainfall at CU campus and Sugarloaf might have been related to the passage of the mesovortex. It developed north of Denver around 0400 UTC and traveled northwestward toward Boulder [Fig. 6 in Friedrich et al. (2015); Morales et al. 2015]. Note that with a 3-km resolution, intrinsically VDRAS is only capable of resolving physical features >20 km and was therefore unable to fully resolve the structure of the mesovortex.

During the second episode, rainfall was also organized in bands of intense rainfall that lasted more than 10 min at the disdrometer sites (Fig. 3). CU campus recorded four maxima with $R > 30 \,\mathrm{mm}\,\mathrm{h}^{-1}$ (denoted as 8–11 in

Fig. 3), while Sugarloaf recorded only one maximum of $R > 30 \,\mathrm{mm}\,\mathrm{h}^{-1}$ (denoted as 12 in Fig. 3). Contrary to the first episode, median convergence and vertical velocity at CU campus and Marshall had almost the same magnitude (Figs. 2c,d). As a result, accumulated rainfall (Table 1) and rainfall intensity at CU campus and Marshall were similar during the second episode, in stark contrast to the large differences seen during the first episode. Maximum convergence was stronger (>0.6 m s⁻¹ km⁻¹) at the lower-elevation stations compared to the higher-elevation stations (<0.5 m s⁻¹ km⁻¹), resulting in lower accumulated rainfall.

Convergence and vertical velocity are not as clearly correlated to the maxima in rainfall in the second episode compared to the first episode (Fig. 7). As summarized by Rotunno and Houze (2007), orographic precipitation is governed by 1) moisture flux toward the mountains, 2) mesoscale orographically induced lift regulated by the shape and steepness of the mountain and the low-level flow characteristics, and 3) precipitation efficiency related to thermodynamic and microphysical processes. Thus, using convergence and vertical velocity as a proxy for maxima in rainfall might address synopticand mesoscale processes. However, precipitation efficiency, advection rate, feedbacks through latent heating or cooling, and smaller-scale processes are not accounted for in the study.

In general, large concentrations of drops with $d < 1.5 \,\mathrm{mm}$ were observed at all times when rain was falling (Fig. 3). After 0000 UTC 12 September, the number concentration shifted toward an increase in medium-sized drops ($d \sim 2\text{-}4\,\mathrm{mm}$), with a corresponding decrease in the concentration of small drops, compared to

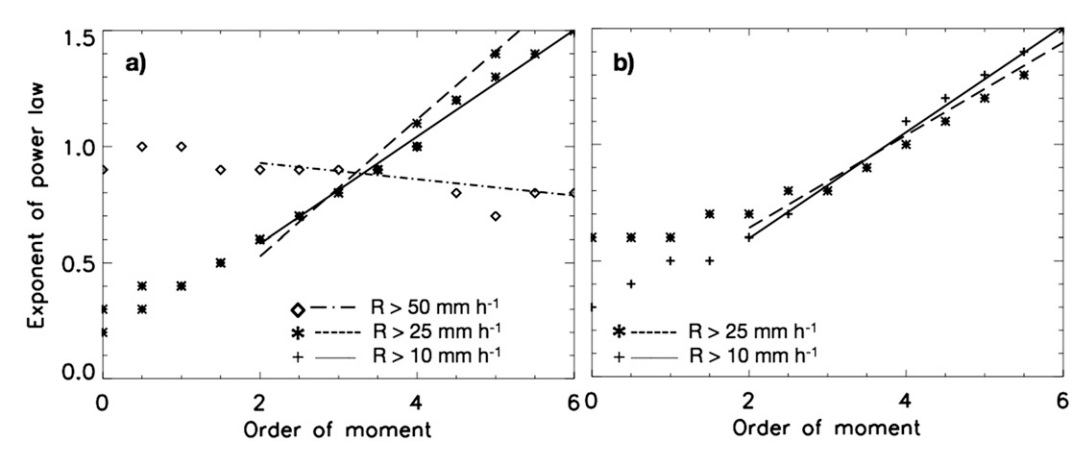


FIG. 8. Global scaling analysis for DSD data observed at CU campus for the (a) first (0000–0800 UTC 12 Sep) and (b) second intensive rain episodes (between 2000 UTC 12 Sep and 0400 UTC 13 Sep). Asterisks and plus signs represent the exponents of the power law between $\log(R)$ and the *m*th order of moments of the DSD (in steps of 0.5). Solid (dashed) lines show the linear regression line for $R > 10 \,\mathrm{mm}\,\mathrm{h}^{-1}$ ($R > 25 \,\mathrm{mm}\,\mathrm{h}^{-1}$); the dash–dotted line shows the linear regression for $R > 50 \,\mathrm{mm}\,\mathrm{h}^{-1}$. Following Uijlenhoet et al. (2003), scaling exponents are only calculated between the second and sixth moment. Scaling exponents are listed in Table 2.

before 0000 UTC and between 0800 and 2000 UTC 12 September, when rainfall was mainly less than 20 mm h⁻¹ at CU campus and Sugarloaf. A slightly larger concentration of medium-sized drops, larger accumulated rainfall, and larger values of liquid water content were observed by the disdrometers at CU campus and Sugarloaf during the first episode (0000-0800 UTC 12 September) compared to the second episode (from 2000 UTC 12 September to 0400 UTC 13 September). The disdrometer at CU campus (Sugarloaf) observed the largest values of W exceeding $1 \,\mathrm{g \, kg^{-1}} \,23\%$ (6%) of the time during the first episode, compared to 11% (0%) of the time during the second episode (Fig. 4). The disdrometer at Marshall observed the largest values of W exceeding 1 g kg⁻¹ 38% of the time during the second episode, compared to 0.4% of the time during the first episode. However, on average, the disdrometers at Marshall and Sugarloaf observed slightly larger W during the first compared to the second episode, with average values of 0.35 $(0.25) \,\mathrm{g\,kg^{-1}}$ compared to 0.19 $(0.17) \,\mathrm{g\,kg^{-1}}$ at Marshall (Sugarloaf).

c. Microphysical considerations

Several studies have identified three microphysical modes that relate rainfall intensity fluctuations to specific variation of DSDs: 1) DSD fluctuation is controlled by a variation in N_T (number controlled with constant μ and D_0), 2) DSD is controlled by a variation in raindrop sizes (size controlled with constant N_T and μ), and 3) DSD is controlled by a mixture of varying drop density and drop sizes (Smith 1993; Smith and Krajewski

1993; Uijlenhoet et al. 2003; Steiner et al. 2004). Number-controlled conditions can be found in warm rain process-dominated environments like tropical rainfall, severe thunderstorms, or persistent intense orographic rainfall. Under those conditions, it is assumed that collision-coalescence processes and raindrop breakup are in balance (e.g., Srivastava 1971; List et al. 1987; Hu and Srivastava 1995; Steiner et al. 2004, and references within). On the other hand, sizecontrolled conditions can be expected in steady stratiform-like drizzle with $R < 1 \,\mathrm{mm}\,\mathrm{h}^{-1}$ similar to the warm rain process-dominated orographic rainfall in Hawaii (Blanchard 1953; Fujiwara 1967). Under those conditions, collision-coalescence and breakup do not play a dominant role in the enhancement and weakening of rainfall. Waldvogel (1974) also related changes in both raindrop size and number density under constant rainfall rates to microphysical conditions. Breakup of raindrops and onset of riming can be expected when D_0 decreases and N_T increases, leading to an increase in N_0 (also referred to as an N_0 jump by Waldvogel). He further associated rapid growth with an increase in coalescence and aggregation, which can be observed as an increase in D_0 and a decrease in N_T and N_0 .

To further assess the dominant processes that contributed to DSD variation, a global scaling analysis following Sempere Torres et al. (1994, 1998) and Uijlenhoet et al. (2003) was performed on the DSDs measured at CU campus during the first and second intensive rain episodes [see Fig. 1 in Uijlenhoet et al. (2003)]. Figure 8 and Table 2 show the global scaling analysis for the DSD data when $R > 10 \,\mathrm{mm}\,\mathrm{h}^{-1}$. The scaling exponents (α, β) for the first and

TABLE 2. Results from the global scaling analysis following Sempere Torres et al. (1994, 1998) and Uijlenhoet et al. (2003) for the first and second intensive rain episodes: scaling components (α, β) , exponent of the power-law Z-R relationship b calculated from scaling components (α, β) as $b = \alpha + 7\beta$, correlation coefficient r^2 between the exponents γ_m of power-law relationships between the mth order moment of the raindrop size distribution (for $0 \le m \le 6$, in steps of 0.5; regression line in Fig. 8), and number of samples n.

	First episode			Second episode	
	$R > 10 \mathrm{mm}\mathrm{h}^{-1}$	$R > 25 \mathrm{mm}\mathrm{h}^{-1}$	$R > 50 \mathrm{mm}\mathrm{h}^{-1}$	$R > 10 \mathrm{mm}\mathrm{h}^{-1}$	$R > 25 \mathrm{mm}\mathrm{h}^{-1}$
α	0.11	-0.06	0.99	0.14	0.24
β	0.23	0.29	-0.03	0.23	0.20
b	1.72	1.97	0.99	1.75	1.80
r^2	0.99	0.98	0.39	0.99	0.97
n	484	191	25	314	70

second episodes are quite similar for $R > 10 \,\mathrm{mm}\,\mathrm{h}^{-1}$ and $R > 25 \,\mathrm{mm}\,\mathrm{h}^{-1}$, resulting in a comparable exponent for the power-law Z-R relationship. Larger values of β suggest the variation of the DSD might be mainly, although not exclusively, controlled by size, which might have been the case for DSDs with $R > 10 \,\mathrm{mm}\,\mathrm{h}^{-1}$ and $R > 25 \,\mathrm{mm}\,\mathrm{h}^{-1}$ during the first and second episodes. With increasing rainfall rates $(R > 50 \,\mathrm{mm}\,\mathrm{h}^{-1})$ and an increase in number concentrations of medium-sized raindrops, β increases toward number-controlled DSDs during the first episode. For DSDs with large rainfall rates $(R > 50 \,\mathrm{mm}\,\mathrm{h}^{-1})$, β decreases rapidly, suggesting that the variations in the DSDs are primarily related to varying raindrop concentrations, which can also be interpreted as an equilibrium between coalescence and raindrop breakup. It seems that the increased convergence yielded enhanced updrafts that effectively converted moisture into rainfall by primarily warm-rain processes at lower levels. This produced high concentrations of small- to moderate-sized raindrops, which the scaling analysis of Uijlenhoet et al. (2003) reveals as "number controlled" fluctuations in DSD. Note that

the confidence limit is quite low for $R > 50 \,\mathrm{mm}\,\mathrm{h}^{-1}$ because of the small sample size.

4. General DSDs characteristics during the first and second episodes

a. Mean size spectra

To further investigate the changes in DSDs between the first and second episodes, mean size spectra of the DSD were derived from 5-min samples. Figure 9a shows the mean raindrop size distribution for the four instrument locations accumulated over the first and second episodes. Overall, the foothills stations Melvina Hill and Sugarloaf observed a larger number of smaller raindrops ($d < 1.5 \, \mathrm{mm}$), while the lower-elevation stations (CU campus and Marshall) observed a larger number of medium- and large-sized drops ($d > 3.2 \, \mathrm{mm}$). At CU campus, the concentration of small drops was similar during the first and second episodes, while larger concentrations of large drops were observed during the first compared to the second episode. At Marshall, concentrations of drops with $d < 2 \, \mathrm{mm}$ were similar

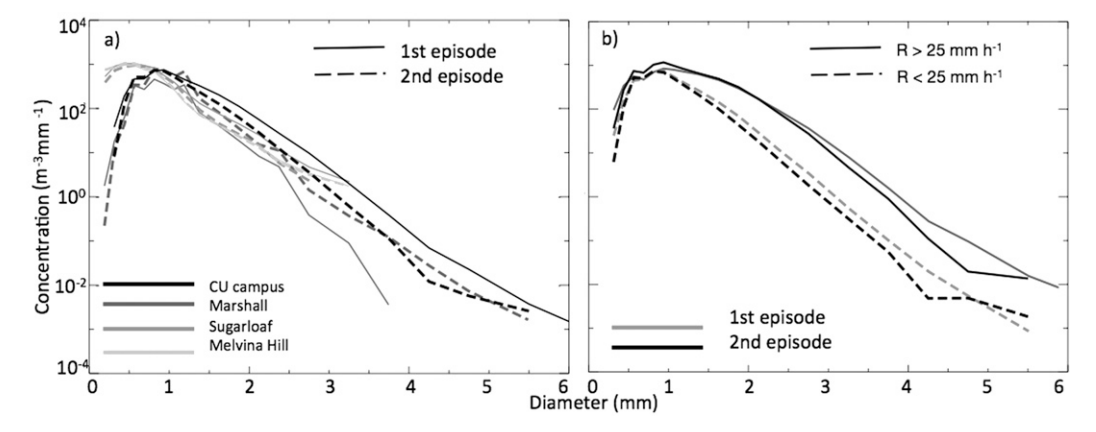


FIG. 9. (a) Mean DSD at CU campus (black lines), Marshall (dark gray lines), Melvina Hill (light gray lines), and Sugarloaf (medium gray lines) during the first (solid lines) and second (dashed lines) intensive rain episodes. (b) Mean DSD at CU campus for rainfall >25 mm h⁻¹ (solid lines) and <25 mm h⁻¹ (dashed lines) occurring during the first (medium gray lines) and second (black lines) intensive rain episodes.

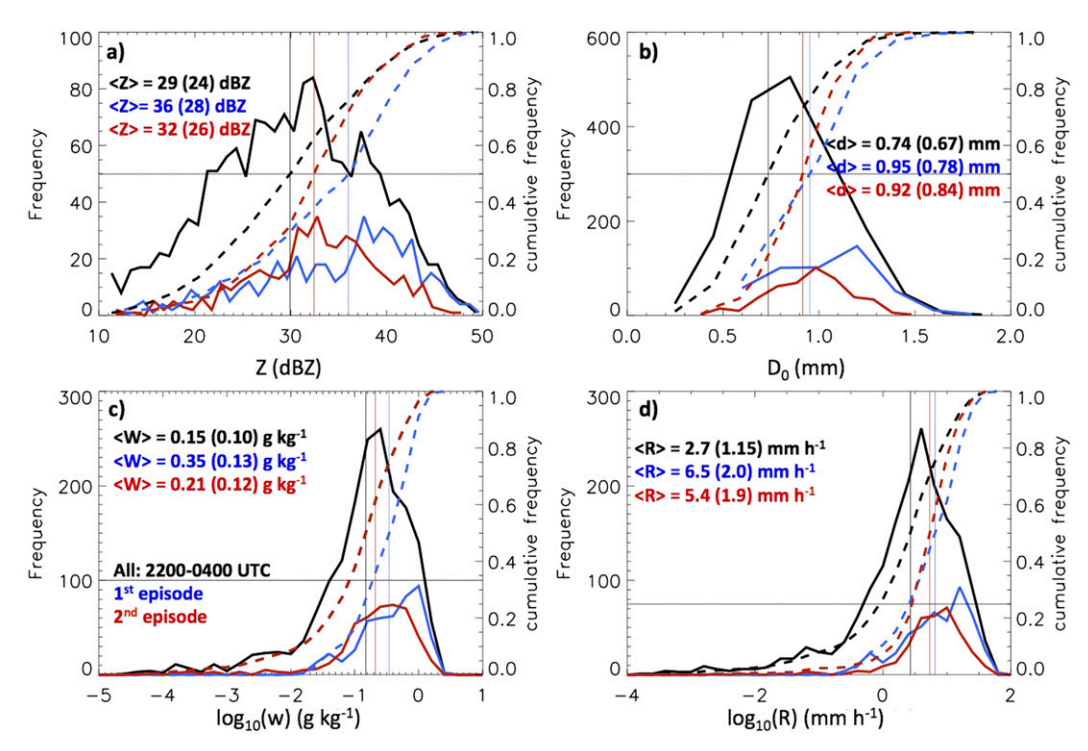


FIG. 10. Frequency distribution (solid lines) and cumulative frequency (dashed lines) of (a) reflectivity, (b) median volume diameter, (c) liquid water content, and (d) rainfall rate based on disdrometer data observed at CU campus during the first (blue) and second intensive rain episodes (red) and the entire episode between 2200 UTC 11 Sep and 0400 UTC 13 Sep (black). Median values are shown with those for Sugarloaf in parentheses.

during the first and second episodes (Fig. 9a). However, the largest concentration of larger drops was observed during the second episode (dashed dark gray line). While the DSDs observed at Marshall and CU campus were quite different during the first episode, the observed concentrations were similar during the second episode. At the higher-elevation stations (Melvina Hill and Sugarloaf) the DSDs have similar shapes. At Sugarloaf, the largest concentration of both small- and medium-sized drops was observed during the first compared to the second episode. At Melvina Hill, the concentrations are almost identical during the first and second episodes.

The difference in DSDs during the intense precipitation periods when $R > 25 \,\mathrm{mm}\,\mathrm{h}^{-1}$ compared to times when $R < 25 \,\mathrm{mm}\,\mathrm{h}^{-1}$ is shown in Fig. 9b based on the data from CU campus. This threshold was chosen to separate the intense rain episodes denoted as 1–12 in Fig. 3 from the rest of the rain during the first and second episodes. During the first and second episodes, the concentration of drops with $d < 1 \,\mathrm{mm}$ was similar for the intense $(R > 25 \,\mathrm{mm}\,\mathrm{h}^{-1})$ and less-intense $(R < 25 \,\mathrm{mm}\,\mathrm{h}^{-1})$ precipitation periods (Fig. 9). Larger concentrations of medium- and large-sized drops $(2 \le d < 4 \,\mathrm{mm})$ were observed during the intense rainfall compared to the less-intense precipitation periods. During

the intensive rainfall periods, larger concentrations of medium- and large-sized drops were observed during the first episode compared to the second episode. In addition, smaller concentrations of small-sized drops $(d < 2 \, \mathrm{mm})$ were observed during the first compared to the second episode.

b. Frequency distributions at CU campus

Although mean size spectra differ between the first and second intensive rain episodes as discussed in section 4a, the question remains as to how the median values of Z, D_0 , W, and R and the gamma fit parameters (N_0 , μ , and Λ) differ between the two intense rainfall episodes. Figure 10 shows the frequency distribution of rain parameters (Z, D_0 , W, and R) at CU campus, which observed the most intense rainfall of the four disdrometer locations. Rain parameters were calculated based on the 1-min values for the entire event (black lines), the first episode (blue lines) with average rainfall rates of 12.2 mm h⁻¹ over 8 h, and the second episode (red lines) with average rainfall rates of 9 mm h⁻¹ over 8 h (Table 1). Median values for the higher-elevation station at Sugarloaf are shown in parentheses in Fig. 10.

The comparison of rain parameters between the first and second episodes revealed slightly larger median reflectivity values (where angle brackets indicate

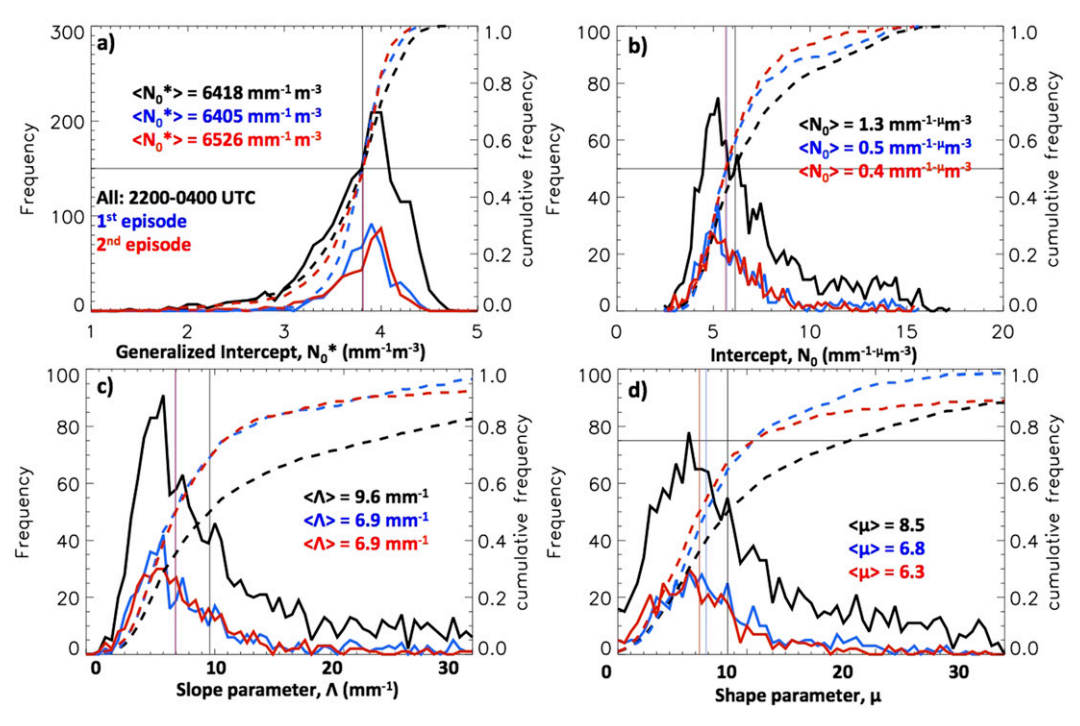


FIG. 11. As in Fig. 10, but for the (a) generalized intercept parameter and the gamma distribution fit parameters, (b) intercept, (c) slope, and (d) shape parameter.

median values; Fig. 10a: $\langle Z \rangle = 36 \, \mathrm{dB} Z$ during the first episode vs $\langle Z \rangle = 32 \, \text{dB}Z$ during the second episode), slightly larger median diameters (Fig. 10b: $\langle d \rangle = 0.95 \,\mathrm{mm}$ during the first episode vs $\langle D \rangle = 0.92 \,\mathrm{mm}$ during second episode), larger median liquid water content (Fig. 10c: $\langle W \rangle = 0.35 \,\mathrm{g \, kg^{-1}}$ during the first episode vs $\langle W \rangle = 0.21 \,\mathrm{g \, kg^{-1}}$ during the second episode), and heavier median rainfall rates (Fig. 10d: $\langle R \rangle = 6.5 \,\mathrm{mm}\,\mathrm{h}^{-1}$ during the first episode vs $\langle R \rangle = 5.4 \,\mathrm{mm} \,\mathrm{h}^{-1}$ during second episode) during the first episode. Median values over the entire 30 h between 2200 UTC 11 September and 0400 UTC 13 September were influenced by DSDs during the 14h of light rain between 0800 and 2000 UTC 12 September (Fig. 4) and, as such, all values were smaller compared to the intense rain episodes (black numbers and lines in Fig. 10). Larger values during the first episode compared to the second episode and the entire period were also observed at the higher-elevation station at Sugarloaf (Fig. 10, values in parentheses), although the median values were much smaller compared to CU campus.

Figure 11 shows the frequency distribution of the intercept, normalized intercept, slope, and shape parameters based on 1-min data observed at CU campus. Fitting the DSD to a gamma distribution shows that the frequency distribution of N_0 , Λ , and μ are similar during the first and second events, with the median value being smaller during the intense rain episodes compared to the

entire event (Figs. 11b–d). This tendency suggests that drops observed during the intense rain episodes were larger in size with a smaller concentration of small-sized drops compared to the entire event. However, the overall shape of the DSDs between the first and second episodes is quite similar, although more convective rainfall with larger concentration of medium-sized drops was observed occasionally during the first episode. The median values of the normalized intercept parameters were quite similar for the first and second episodes as well as for the entire event (Fig. 11a).

c. Z-R relationships

Now that we showed that DSDs, rainfall parameters, and the gamma function parameters differ between the first and second episodes, one may wonder how that affects the Z-R relationship. The 1-min-sample DSDs from CU campus were used to compute Z-R relationships for the entire event and the first and second episodes (Fig. 12). Note that time averaging and sample size notably affect the Z-R relationship, as shown by Steiner and Smith (2000, 2004). Heavier rainfall and higher reflectivity occurred during the first episode compared to the second episode. During the first episode, $R > 10 \, \mathrm{mm \, h^{-1}}$ was observed over 148 min and $R > 25 \, \mathrm{mm \, h^{-1}}$ was observed over 82 min. The maximum rainfall rate during the first episode was 71 mm $\mathrm{h^{-1}}$. A large spread in rainfall rates from 0.01 to 10 mm $\mathrm{h^{-1}}$

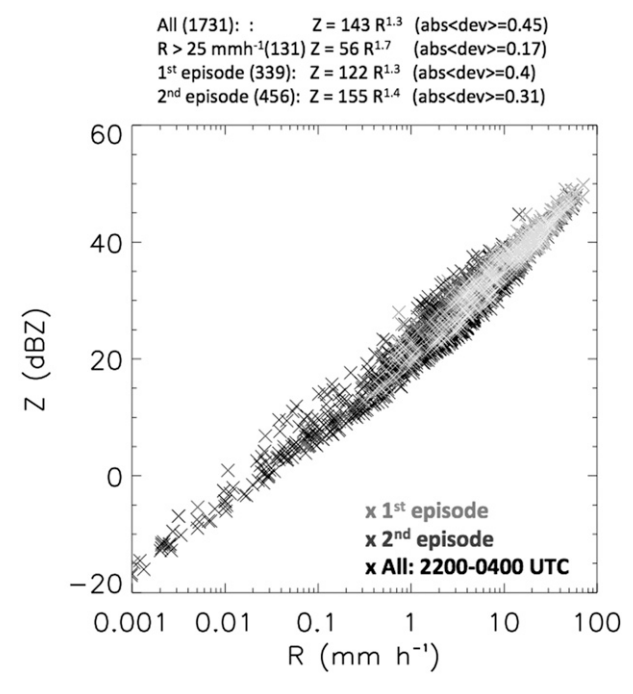


FIG. 12. Scatterplots of Z–R from DSD datasets measured at CU campus every minute for the first (light gray crosses) and second intensive rain episodes (dark gray crosses), and during the entire event (black cross signs). The regression shown above was computed between log(R) and log(Z) using a least-absolute-deviation fit. The mean of the absolute deviation is indicated in parentheses.

with maximum rainfall of $59 \,\mathrm{mm} \,\mathrm{h}^{-1}$ occurred during the second episode. Intense rainfall with $R > 25 \,\mathrm{mm} \,\mathrm{h}^{-1}$ was observed over $33 \,\mathrm{min}$, while $R > 10 \,\mathrm{mm} \,\mathrm{h}^{-1}$ occurred over $155 \,\mathrm{min}$ during the second episode. As a result, the Z-R ($Z=aR^b$; with a and b being empirical constants) relationships for the first and second episodes are quite different, with a=122 compared to a=155 during the second episode. Interestingly, the Z-R relationship derived from the data observed over $131 \,\mathrm{min}$ of intense rain ($R > 25 \,\mathrm{mm} \,\mathrm{h}^{-1}$) revealed a much smaller a (a=56) and a higher b value compared to values derived during the

first and second episodes and the entire event. Nevertheless, these a values were much smaller than the values of the "standard" NEXRAD Z-R relationship for nontropical convective precipitation (Z = $300R^{1.4}$), resulting in an underestimation of radarbased rainfall by 29%-36% at CU campus as shown in Table 3. Table 3 compares the accumulated rainfall based on the disdrometer observations with the R derived from various Z-R relationships using the disdrometer-based Z. The a values during the second episode were closer to the Z-R relations sometimes used for orographic precipitation by the WSR-88D network ($Z = 200R^{1.6}$; Marshall and Palmer 1948). The larger exponent in the Marshall–Palmer relationship still yielded an underestimation of rainfall (36%–38%). Interestingly, the Z-R relationship for tropical rain events ($Z = 250R^{1.2}$; Rosenfeld et al. 1993) yielded an overestimation of rainfall at CU campus (10%-34%).

5. Discussion

a. Importance of DSDs for rainfall nowcasting

As shown in section 4c, the standard NEXRAD Z-Rrelationship for nontropical rainfall underestimated rainfall by over 30%. In addition, the dominance of mainly small spherical raindrops resulted in low differential signal between the horizontal and vertical polarization, making it difficult to use dual-polarization variables such as Z_{dr} and K_{dp} for accurate rain-rate estimation. Figure 13 shows the relationship between radar- and disdrometer-based Z_{dr} , K_{dp} , and reflectivity derived over CU campus. While both systems suffer from large uncertainties and errors, which we will not address here, both reveal the same trend of small $Z_{\rm dr}$ and K_{dp} values. For more information on uncertainties and errors sources of dual-polarization measurements and T-matrix retrieval algorithm, see Ryzhkov and Zrnić (1995), Ryzhkov et al. (2005a,b,c), Vivekanandan et al. (1991), Bringi and Chandrasekar (2001), and Kalina et al. (2014, and references therein). The radar-based dual-polarization variables were

TABLE 3. Rainfall accumulations observed by the disdrometer at CU campus for the first and second intensive rain episodes and the entire event from 2200 UTC 11 Sep to 0400 UTC 13 Sep. The disdrometer-observed Z values are used as input to the NEXRAD Z-R relationships, which are commonly used by the operational radars. Percentages of the disdrometer-observed accumulations are shown in parentheses.

	Accumulated <i>R</i> from disdrometers (mm)	Accumulated R using Z from the disdrometer and $Z = 300R^{1.4}$	Accumulated R using Z from the disdrometer and $Z = 200R^{1.6}$	Accumulated R using Z from the disdrometer and $Z = 250R^{1.6}$
First episode	107.8	76.3 (71%)	69.1 (64%)	144.1 (134%)
Second episode	71.6	46.1 (64%)	44.9 (63%)	79.2 (110%)
From 2200 UTC 11 Sep to 0400 UTC 13 Sep	233.1	150.5 (64%)	145.1 (62%)	264.3 (113%)

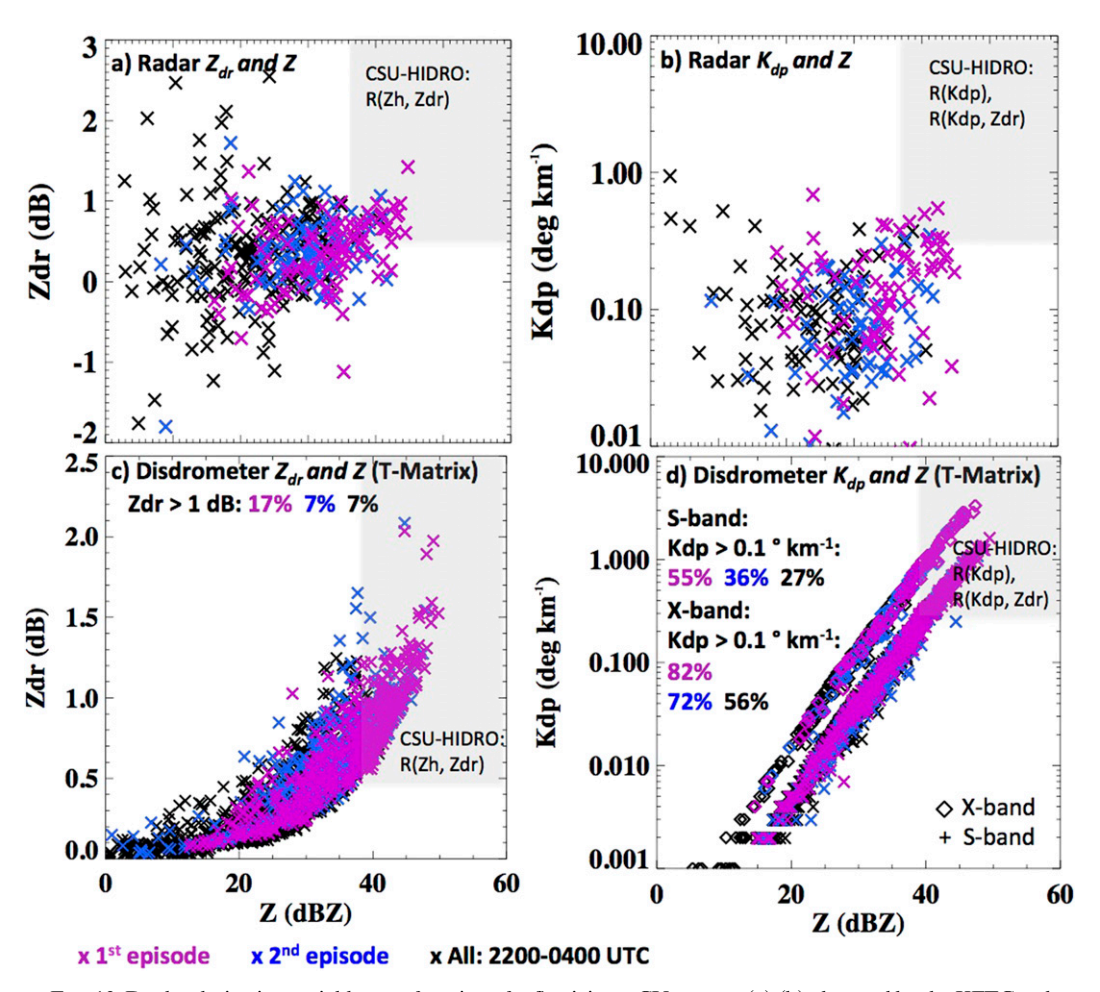


FIG. 13. Dual-polarization variables as a function of reflectivity at CU campus (a),(b) observed by the KFTG radar at 0.5° elevation angle and (c),(d) derived from the disdrometer observations using the T-matrix scattering program: (left) $Z_{\rm dr}$ and (right) $K_{\rm dp}$ as a function of Z for the first (magenta crosses) and second (blue crosses) intensive rain episodes and the entire episode (black crosses) between 2200 UTC 11 Sep and 0400 UTC 13 Sep. In (d), $K_{\rm dp}$ values were derived for S- (crosses) and X-band (diamonds) wavelengths. Gray shading indicates times when dual-polarization values could have been used for rain-rate estimation based on the CSU-HIDRO algorithm.

mainly less than 1 dB (1° km⁻¹). The disdrometer-based dual-polarization variables, which were derived from the T-matrix scattering program, support the radar observations. Larger oblate droplets with larger $Z_{\rm dr}$ (>1 dB) and $K_{\rm dp}$ (>1° km⁻¹) were observed primarily during the first episode. Nevertheless, only 17% (55%) of the 1-min data that were observed during the first episode showed a significant signal with $Z_{\rm dr} > 1\,{\rm dB}$ $(K_{\rm dp} > 1^{\circ} \, {\rm km}^{-1})$. As a result, rainfall algorithm methods such as the Colorado State University-Hydrometeor Identification Rainfall Optimization (CSU-HIDRO; Cifelli et al. 2011) or the National Severe Storms Laboratory (NSSL) algorithm developed during the Joint Polarization Experiment (JPOLE; Ryzhkov et al. 2005b,c), which both use dual-polarization variables to determine rain rate, were unable to fully utilize the dual-polarization

capability. For example, following the criteria of the CSU-HIDRO algorithm [see Fig. 3 in Cifelli et al. (2011)], only 2% (11%) of the radar (disdrometer) data for the entire event would meet the criteria for using either the $R(K_{dp})$ or $R(K_{\rm dp},\ Z_{\rm dr})$ algorithm and 30% (23%) of the radar (disdrometer) data for the entire event would qualify for use of the $R(Z_{dr})$ algorithm for rain-rate estimation during the entire event between 2200 UTC 11 September and 0400 UTC 13 September. Theoretical modeling with experimental raindrop size distributions indicates that because of non-Rayleigh resonance effects, K_{dp} values at X band are, on average, a factor of 3.7 greater than at S band (Matrosov et al. 2006). Therefore, K_{dp} measurements at X band are less noisy and larger compared to K_{dp} measurements at S band for light rainfall, as shown when comparing disdrometer-based K_{dp} at S

versus X band (Fig. 13d). Since, K_{dp} at X band is greater than at S band, slightly more time steps could have been used for rainfall estimation when an X-band radar had been deployed during the Great Colorado Flood. Since the standard radar-based rainfall algorithms derived rainfall that was much less than rainfall observed by rain gauges, the question remains how important DSD observations may be for rainfall nowcasting applications. Several studies have already emphasized the importance of capturing the spatial and temporal variability of DSD using disdrometers in addition to radars (e.g., Miriovsky et al. 2004; Lee and Zawadzki 2005; Lee et al. 2007). Certainly, during the Great Colorado Flood, disdrometer observations could have helped explaining the discrepancy between rainfall derived by radar and observed by rain gauges.

b. Comparison of DSDs characteristics to other events

Many studies have combined dynamical (stratiform vs convective) and microphysical (continental vs maritime) processes to explain the variation of DSDs within a storm, between storms, and across climate regimes (e.g., Fabry and Zawadzki 1995; Waldvogel et al. 1995; Barthazy et al. 1998; Steiner and Smith 1998; Uijlenhoet et al. 2003; Bringi et al. 2003; Dolman et al. 2011; Munchak et al. 2012, and references therein). However, the coupling between dynamical and microphysical processes is highly complex because of the feedback of latent heat release and/or cooling on the dynamics and microphysics (Miltenberger et al. 2015). Larger concentrations of smaller-sized raindrops (diameters <2 mm), similar to what was observed during the Great Colorado Flood, have been observed primarily in tropical regions (e.g., Amazon of Brazil, Florida, and Kwajelein Island) where warm-rain formation processes dominate (Tokay and Short 1996; Carey et al. 2001; Bringi et al. 2003; Munchak et al. 2012). For instance, Tokay and Short (1996) analyzed ~127 h of disdrometer observations from the Tropical Ocean and Global Atmosphere Coupled Ocean-Atmosphere Response Experiment (TOGA COARE; Webster and Lukas 1992). Larger concentrations of small- to medium-sized drops ($2 \le d < 4$ mm) with fewer larger drops ($d \ge 4$ mm) were observed during convective events accompanied by an increase in liquid water content and a decrease in medium volume diameter and reflectivity. As a result, radar reflectivity-rainfall relationships $(Z = aR^b)$ showed smaller intercept parameters (i.e., a) and larger exponents (i.e., b) compared to stratiform raindrop spectra (e.g., Steiner and Smith 1998). During the Great Colorado Flood, the intercept parameters derived from the DSDs (56 < a < 155) were also much smaller compared to the intercept parameters used for the standard Z-R relationship in the midlatitudes (200 < a < 300). Large concentrations of smallto medium-sized raindrops have also been observed in orographic rainfall; for example, during the 1997 Fort Collins flood (Petersen et al. 1999; Bringi et al. 2003), along the California coast (Martner et al. 2008), and in Hawaii (Blanchard 1953). Martner et al. (2008) observed shallow warm rain (also referred to as nonbrightband rain) along the California coast, which produced rainfall rates up to $10 \, \mathrm{mm} \, \mathrm{h}^{-1}$. They also concluded that because of the large concentration of small raindrops, the Z-R relationship changes to Z = $56R^{1.6}$ for nonbrightband rain compared to Z = $166R^{1.6}$ for clouds extending far above the melting layer.

6. Conclusions

Drop size distributions observed by four PARSIVEL disdrometers during the Great Colorado Flood from 11 to 13 September 2013 at two stations in the foothills (Melvina Hill and Sugarloaf) and two stations located on the plains east of the foothills (Marshall and CU campus) were examined. DSD parameters $(R, Z, D_0,$ and W) and gamma distribution parameters were derived and compared between the foothills and plains locations during different rainfall episodes. In contrast to Friedrich et al. (2015), where the spatial and temporal distributions of radar variables were emphasized, this study focused on changes in disdrometer-measured drop size distributions as a function of location, altitude, and time.

Rainfall throughout the entire event was characterized by a large number of small- to medium-sized raindrops ($d < 1.5 \,\mathrm{mm}$), resulting in small values of $Z(<40\,\mathrm{dB}Z)$ and $D_0(<1\,\mathrm{mm})$. In addition, high moisture content was present throughout the entire event. While high moisture content is not so unusual for heavy rain events in Colorado, the longevity (several days) of high moisture is unusual in Colorado (e.g., Gochis et al. 2015). Raindrops observed at the lower-elevation stations were generally larger compared to those in the foothills. DSDs observed in the foothills were characterized by larger concentrations of small-sized drops ($d < 1 \,\mathrm{mm}$). The first and second intense rainfall episodes showed substantial differences in the wind fields with stronger convergence and vertical velocity observed during the first episode. The dynamical forcing is also reflected in the DSDs. Larger raindrops ($d \sim 1$ –2.5 mm; Fig. 4b) were observed during the convective phase (0300–0500 UTC 12 September) of the first intensive rain episode when deeper clouds, lightning, and supercooled liquid were observed compared to the rest of the first episode and the second episode.

The heaviest rainfall rates ($>40 \,\mathrm{mm}\,\mathrm{h}^{-1}$), with total accumulated rainfall of 113 mm over 8 h at CU campus, occurred during the first intense rainfall episode. Times of intense rainfall were linked to several low-level convergence zones and a mesovortex. The center of the mesoscale circulation approached the observational domain around 0300 UTC and continued to move northwestward. During the early hours, the circulation generated deep convective clouds and periods with intense rainfall at CU campus $(R > 25 \,\mathrm{mm}\,\mathrm{h}^{-1})$ and Marshall $(R > 15 \,\mathrm{mm}\,\mathrm{h}^{-1})$. Later (after 0600 UTC), the circulation moved farther northwestward and intense rainfall $(R > 20 \,\mathrm{mm}\,\mathrm{h}^{-1})$ was observed at Melvina Hill and Sugarloaf. Rainfall rates at the higher-elevation stations were lighter compared to the values observed at CU campus and Marshall. A global scaling analysis revealed how the DSD fluctuations were controlled by changes in drop sizes and number concentration. During the first episode, the controlling mechanism for the DSDs changed from primarily, but not exclusively, size controlled (R >10, $25 \,\mathrm{mm}\,\mathrm{h}^{-1}$) to number controlled ($R > 50 \,\mathrm{mm}\,\mathrm{h}^{-1}$), with deeper convective rain being primarily number controlled.

The second episode led to smaller total accumulated rainfall of 70 mm over 8 h at Sugarloaf and 80 mm (70 mm) at CU campus (Marshall). Times of intense rainfall were linked to several low-level convergence zones. Rainfall parameters (Z, D_0 , W, and R) were slightly smaller compared to the first episode. Values at the foothills stations were even smaller compared to the lower-elevation stations. During the second episode, the DSDs with $R > 25 \,\mathrm{mm}\,\mathrm{h}^{-1}$ at CU campus were primarily number controlled, resembling conditions in warm rain-dominated environments with similar DSDs and rainfall rates at the lower-elevation stations. The latter might be related to the location and strength of the low-level convergence zones.

The disdrometer-derived Z-R relations and radar variables reflect how unusual the DSD was during the 2013 Great Colorado Flood. As a result, Z-R relations commonly used by operational NEXRAD strongly underestimated rainfall rate by up to 26%-38% at CU campus, and the signals in the dualpolarization radar variables were too weak to be useful for rain-rate estimations. Even though the Great Colorado Flood was an outlier event compared to other floods in Colorado, these findings are noteworthy since they show the strong effects of low-level convergence zones on precipitation formation and also rainfall estimation because of peculiar raindrop size spectra. The rainfall types and the distribution of intense rainfall strongly depended on the strength and location of the low-level convergence and how it interacted with the terrain. Since enough moisture was available, the depth of the clouds and the microphysical processes primarily depended on the vertical velocity, that is, to which altitudes the moisture was lifted. The large availability of moisture prevented small drops from evaporating before they reached the surface, which under normal conditions in Colorado would have evaporated. The persistent production of small drops allowed for large amounts of precipitation to be generated. The question remains whether the large concentration of small drops and the lack of medium-sized drops at the foothills stations were due to spatial variability (i.e., how far convergence zones may travel into the valleys and how they interact with the mountains), high number concentrations that led to high drop interaction (collisions) that limited drop size (larger drops would break up), or the distance between the melting layer and the ground. Future studies should identify the role of lowlevel convergence on the precipitation formation in the mountains. It would be interesting to determine the degree to which observations may be able to quantify and track low-level convergence and assess how well numerical models might reproduce the kinematic field.

Acknowledgments. The authors thank the organizations, technicians, scientists, and students who have supported the instrument facilities that are used in this analysis. In particular, we thank Scott Kittelman, who maintains the instruments at the ATOC Skywatch Observatory; the staff at the University of Colorado Mountain Research Station; and the staff at the NCAR Marshall facility. This work was supported in part by the U.S. National Science Foundation through its support of NCAR and by the University of Colorado. Any opinions, findings, or recommendations expressed in this publication are those of the authors and do not necessarily reflect the views of the National Science Foundation.

APPENDIX

Comparison among Disdrometer, Rain Gauges, and Radar

Several studies have addressed the sampling uncertainties related to the PARSIVEL disdrometer. Jaffrain and Berne (2011) determined the sampling uncertainty of R and D_0 as a function of temporal resolution. Based on that study, the relative sampling uncertainty for a 1-min sampling interval of R (D_0) ranging between 10 and 20 mm (1–1.5 mm) was about 10%–12% (6%–7%). Comparisons between the first- and second-generation PARSIVEL with a Joss–Waldvogel

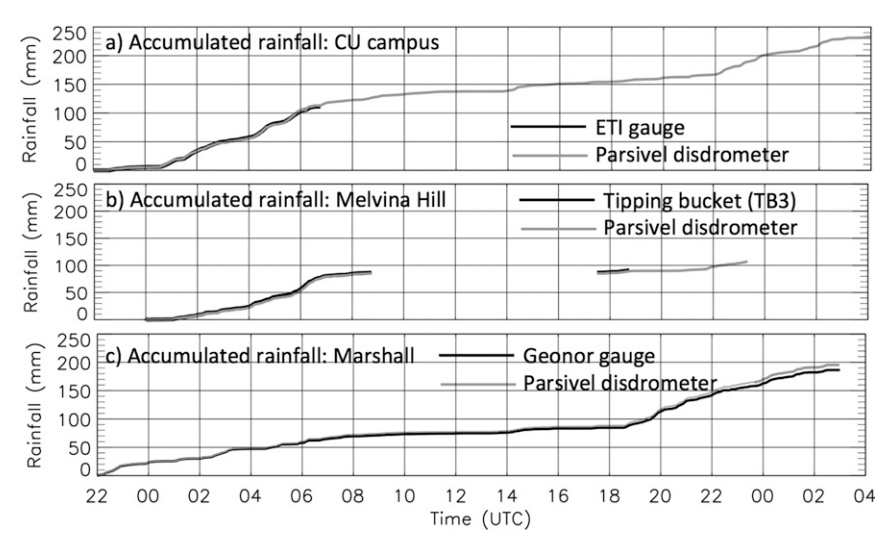


FIG. A1. (a)–(c) Accumulated rainfall at CU campus, Melvina Hill, and Marshall sites between 2200 UTC 11 Sep and 0400 UTC 13 Sep. Gray lines indicate measurements obtained by the disdrometer and black lines indicate measurements from a collocated rain gauge.

disdrometer and rain gauges conducted by Tokay et al. (2014) revealed that the first-generation PARSIVEL disdrometers underestimate (overestimate) drop concentrations for $d < 0.76 \,\mathrm{mm}$ ($d > 2.4 \,\mathrm{mm}$). To validate the quality of the PARSIVEL disdrometer observations,

accumulated disdrometer-based rainfall measurements were compared to rain gauge observations from collocated rain gauges for the observation period, as shown in Fig. A1. Rainfall measurements from the disdrometers located on CU campus and Melvina Hill agree well with

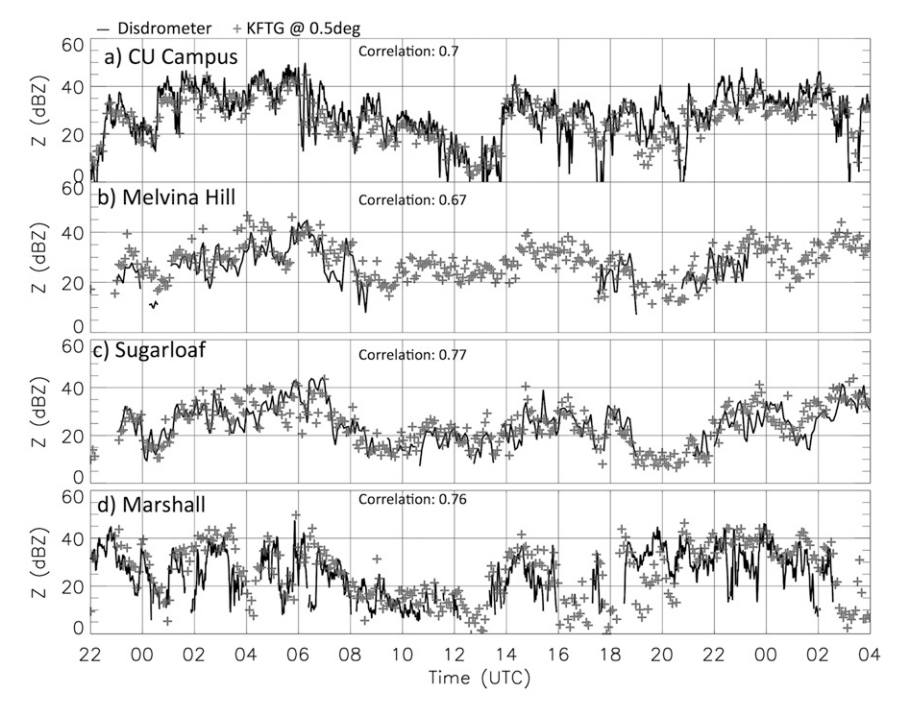


FIG. A2. Reflectivity measurements at four disdrometer sites at (a) CU campus, (b) Melvina Hill, (c) Sugarloaf, and (d) Marshall between 2200 UTC 11 Sep and 0400 UTC 13 Sep. Data include radar reflectivity over the instrument site measured by the Denver NEXRAD at 0.5° elevation angle (gray plus signs) and reflectivity derived from the PARSIVEL disdrometer DSDs (solid black lines). The center of the radar beam at 0.5° elevation angle is located at 590 m AGL at CU campus, 440 m AGL at Marshall, 125 m AGL at Melvina Hill, and 80 m AGL at Sugarloaf.

the ETI weighting gauge and the Hydrological Services tipping-bucket rain gauge (Figs. A1a,b). Note that the ETI gauge at CU campus stopped recording after 0700 UTC 12 September, while the tipping-bucket gauge did not operate between 0900 and 1700 UTC 12 September and after 1900 UTC 12 September. The PARSIVEL disdrometer located at the NCAR Marshall site observed the same general trend in rainfall as the Geonor rain gauge. Accumulated rainfall based on the rain gauge is about ~9 mm (5%) lower compared to the disdrometer.

In addition to the rain gauge data, the reflectivity derived from the disdrometer data is compared to the reflectivity measured by the KFTG radar (Fig. A2; black lines and gray plus signs). The radar reflectivity at the lowest elevation angle at 0.5° was averaged over an array of 3 × 3 radar range gates centered on the instrument site. Even though the radar reflectivity is occasionally off by a few decibels, the increase and decrease in reflectivity as the rainbands passed over the instruments are well represented by the disdrometer measurements. The correlation coefficient between the radar reflectivity and the disdrometer-based reflectivity ranges between 0.6 (Marshall) and 0.7 (CU campus). Note that the radar covers an area of $0.75 \,\mathrm{km} \times 1.6 \,\mathrm{km}$ (3 × 0.25 km in range and 3° × 0.5° in azimuth). In addition, the lowest elevation is prone to contamination from ground clutter.

REFERENCES

- Barthazy, E., W. Henrich, and A. Waldvogel, 1998: Size distribution of hydrometeors through the melting layer. *Atmos. Res.*, **47–48**, 193–208, doi:10.1016/S0169-8095(98)00065-9.
- Beard, K. V., and C. H. Chuang, 1987: A new model for the equilibrium shape of raindrops. J. Atmos. Sci., 44, 1509–1524, doi:10.1175/1520-0469(1987)044<1509:ANMFTE>2.0.CO;2.
- Blanchard, D. C., 1953: Raindrop size-distribution in Hawaiian rains. J. Meteor., 10, 457–473, doi:10.1175/1520-0469(1953)010<0457: RSDIHR>2.0.CO;2.
- Bringi, V. N., and V. Chandrasekar, 2001: Polarimetric Doppler Weather Radar: Principles and Applications. Cambridge University Press, 662 pp.
- —, —, J. Hubbert, E. Gorgucci, W. L. Randeu, and M. Schoenhuber, 2003: Raindrop size distribution in different climatic regimes from disdrometer and dual-polarized radar analysis. J. Atmos. Sci., 60, 354–365, doi:10.1175/1520-0469(2003)060<0354: RSDIDC>2.0.CO;2.
- Carey, L. D., R. Cifelli, W. A. Petersen, S. A. Rutledge, and M. A. F. S. Dias, 2001: Characteristics of Amazonian rain measured during TRMM-LBA. Preprints, 30th Conf. on Radar Meteorology, Munich, Germany. Amer. Meteor. Soc., 12A.9. [Available online at http://ams.confex.com/ams/30radar/techprogram/paper_21229.htm.]
- Cifelli, R., V. Chandrasekar, S. Lim, P. C. Kennedy, Y. Wang, and S. A. Rutledge, 2011: A new dual-polarization radar rainfall algorithm: Application in Colorado precipitation events. *J. Atmos. Oceanic Technol.*, 28, 352–364, doi:10.1175/2010JTECHA1488.1.

- Crook, N. A., and J. Sun, 2002: Assimilating radar, surface, and profiler data for the Sydney 2000 forecast demonstration project. *J. Atmos. Oceanic Technol.*, **19**, 888–898, doi:10.1175/1520-0426(2002)019<0888:ARSAPD>2.0.CO;2.
- Dolman, B. K., P. T. May, I. M. Reid, and R. A. Vincent, 2011:
 Profiler retrieved DSD evolution in the tropics and midlatitudes. Preprints, 35th Conf. on Radar Meteorology,
 Pittsburgh, PA. Amer. Meteor. Soc., 8A.1. [Available online at https://ams.confex.com/ams/35Radar/webprogram/Paper191545.html.]
- Fabry, F., and I. Zawadzki, 1995: Long-term radar observations of the melting layer of precipitation and their interpretation. *J. Atmos. Sci.*, **52**, 838–851, doi:10.1175/1520-0469(1995)052<0838: LTROOT>2.0.CO;2.
- Friedrich, K., S. Higgins, F. J. Masters, and C. R. Lopez, 2013a: Articulating and stationary PARSIVEL disdrometer in severe weather. J. Atmos. Oceanic Technol., 30, 2063–2080, doi:10.1175/ JTECH-D-12-00254.1.
- ——, E. A. Kalina, F. J. Masters, and C. R. Lopez, 2013b: Drop-size distributions in thunderstorms measured by optical disdrometers during VORTEX2. *Mon. Wea. Rev.*, **141**, 1182–1203, doi:10.1175/ MWR-D-12-00116.1.
- —, —, J. Aikins, D. Gochis, and R. Rasmussen, 2015: Precipitation and cloud structures of intense rain during the 2013 Great Colorado Flood. J. Hydrometeor., 17, 27–52, doi:10.1175/JHM-D-14-0157.1.
- Fujiwara, M., 1967: Raindrop size distribution in warm rain as measured in Hawaii. *Tellus*, 19, 392–402, doi:10.1111/ j.2153-3490.1967.tb01494.x.
- Gochis, D., and Coauthors, 2015: The Great Colorado Flood of September 2013. Bull. Amer. Meteor. Soc., 96, 1461–1487, doi:10.1175/BAMS-D-13-00241.1.
- Hu, Z., and R. C. Srivastava, 1995: Evolution of raindrop size distribution by coalescence, breakup, and evaporation: Theory and observations. *J. Atmos. Sci.*, **52**, 1761–1783, doi:10.1175/1520-0469(1995)052<1761:EORSDB>2.0.CO;2.
- Jaffrain, J., and A. Berne, 2011: Experimental quantification of the sampling uncertainty associated with measurements from PARSIVEL disdrometers. J. Hydrometeor., 12, 352–370, doi:10.1175/ 2010JHM1244.1.
- Joss, J., and A. Waldvogel, 1967: Ein Spektrograph für Niederschlagstropfen mit automatischer Auswertung. *Pure Appl. Geophys.*, 68, 240–246, doi:10.1007/BF00874898.
- Kalina, E. A., K. Friedrich, S. M. Ellis, and D. W. Burgess, 2014: Comparison of disdrometer and X-band mobile radar observations in convective precipitation. *Mon. Wea. Rev.*, 142, 2414–2435, doi:10.1175/MWR-D-14-00039.1.
- Krajewski, W. F., and Coauthors, 2006: DEVEX-disdrometer evaluation experiment: Basic results and implications for hydrologic studies. Adv. Water Resour., 29, 311–325, doi:10.1016/ j.advwatres.2005.03.018.
- Lee, G. W., and I. Zawadzki, 2005: Variability of drop size distributions: Time-scale dependence of the variability and its effects on rain estimation. *J. Appl. Meteor.*, 44, 241–255, doi:10.1175/JAM2183.1.
- ——, A. W. Seed, and I. Zawadzki, 2007: Modeling the variability of drop size distributions in space and time. *J. Appl. Meteor. Climatol.*, 46, 742–756, doi:10.1175/JAM2505.1.
- List, R., N. R. Donaldson, and R. E. Stewart, 1987: Temporal evolution of drop spectra to collisional equilibrium in steady and pulsating rain. *J. Atmos. Sci.*, **44**, 362–372, doi:10.1175/1520-0469(1987)044<0362:TEODST>2.0.CO;2.
- Löffler-Mang, M., and J. Joss, 2000: An optical disdrometer for measuring size and velocity of hydrometeors. J. Atmos. Oceanic

- *Technol.*, **17**, 130–139, doi:10.1175/1520-0426(2000)017<0130: AODFMS>2.0.CO;2.
- ——, and U. Blahak, 2001: Estimation of the equivalent radar reflectivity factor from measured snow size spectra. *J. Appl. Meteor.*, 40, 843–849, doi:10.1175/1520-0450(2001)040<0843: EOTERR>2.0.CO;2.
- Marshall, J. S., and W. McK. Palmer, 1948: The distribution of raindrops with size. *J. Meteor.*, **5**, 165–166, doi:10.1175/1520-0469(1948)005<0165:TDORWS>2.0.CO:2.
- Martner, B. E., S. E. Yuter, A. B. White, S. Y. Matrosov, D. E. Kingsmill, and F. M. Ralph, 2008: Raindrop size distributions and rain characteristics in California coastal rainfall for periods with and without a radar bright band. *J. Hydrometeor.*, 9, 408–425, doi:10.1175/2007JHM924.1.
- Matrosov, S. Y., R. Cifelli, P. C. Kennedy, S. Nesbitt, S. A. Rutledge, V. N. Bringi, and B. E. Martner, 2006: A comparative study of rainfall retrievals based on specific differential phase shifts at X- and S-band radar frequencies. *J. Atmos. Oceanic Technol.*, 23, 952–963, doi:10.1175/JTECH1887.1.
- Miltenberger, A. K., A. Seifert, H. Joss, and H. Wernli, 2015: A scaling relation for warm-phase orographic precipitation: A Lagrangian analysis for 2D mountains. *Quart. J. Roy. Meteor. Soc.*, 141, 2185–2198, doi:10.1002/qj.2514.
- Miriovsky, B. J., and Coauthors, 2004: An experimental study of small-scale variability of radar reflectivity using disdrometer observations. J. Appl. Meteor., 43, 106–118, doi:10.1175/ 1520-0450(2004)043<0106:AESOSV>2.0.CO;2.
- Morales, A., R. Schumacher, and S. Kreidenweis, 2015: Mesoscale vortex development during extreme precipitation: Colorado, September 2013. Mon. Wea. Rev., doi:10.1175/ MWR-D-15-0086.1, in press.
- Munchak, S. J., C. D. Kummerow, and G. Elsaesser, 2012: Relationships between the raindrop size distribution and properties of the environment and clouds inferred from TRMM. J. Climate, 25, 2963–2978, doi:10.1175/JCLI-D-11-00274.1.
- Nešpor, V., W. F. Krajewski, and A. Kruger, 2000: Wind-induced error of raindrop size distribution measurement using a two-dimensional video disdrometer. *J. Atmos. Oceanic Tech*nol., 17, 1483–1492, doi:10.1175/1520-0426(2000)017<1483: WIEORS>2.0.CO;2.
- Petersen, W. A., and Coauthors, 1999: Mesoscale and radar observations of the Fort Collins flash flood of 28 July 1997. *Bull. Amer. Meteor. Soc.*, **80**, 191–216, doi:10.1175/1520-0477(1999)080<0191: MAROOT>2.0.CO;2.
- Rasmussen, R., and Coauthors, 2012: How well are we measuring snow: The NOAA/FAA/NCAR winter precipitation test bed. Bull. Amer. Meteor. Soc., 93, 811–829, doi:10.1175/ BAMS-D-11-00052.1.
- Rosenfeld, D., D. B. Wolff, and D. Atlas, 1993: General probability-matched relations between radar reflectivity and rain rate. *J. Appl. Meteor.*, **32**, 50–72, doi:10.1175/1520-0450(1993)032<0050: GPMRBR>2.0.CO;2.
- Rotunno, R., and R. A. Houze, 2007: Lessons on orographic precipitation from the Mesoscale Alpine Programme. *Quart. J. Roy. Meteor. Soc.*, **133**, 811–830, doi:10.1002/qj.67.
- Ryzhkov, A. V., and D. S. Zrnić, 1995: Comparison of dual-polarization radar estimators of rain. J. Atmos. Oceanic Technol., 12, 249–256, doi:10.1175/1520-0426(1995)012<0249: CODPRE>2.0.CO;2.
- —, S. E. Giangrande, V. M. Melnikov, and T. J. Schuur, 2005a: Calibration issues of dual-polarization radar measurements. J. Atmos. Oceanic Technol., 22, 1138–1155, doi:10.1175/ JTECH1772.1.

- —, —, and T. J. Schuur, 2005b: Rainfall estimation with a polarimetric prototype of WSR-88D. J. Appl. Meteor., 44, 502–515, doi:10.1175/JAM2213.1.
- —, T. J. Schuur, D. W. Burgess, P. L. Heinselman, S. E. Giangrande, and D. S. Zrnic, 2005c: The Joint Polarization Experiment: Polarimetric rainfall measurements and hydrometeor classification. *Bull. Amer. Meteor. Soc.*, **86**, 809–824, doi:10.1175/BAMS-86-6-809.
- Sempere Torres, D., J. M. Porrà, and J.-D. Creutin, 1994: A general formulation for raindrop size distribution. *J. Appl. Meteor.*, **33**, 1494–1502, doi:10.1175/1520-0450(1994)033<1494: AGFFRS>2.0.CO;2.
- —, —, and —, 1998: Experimental evidence of a general description for raindrop size distribution properties. *J. Geophys. Res.*, **103**, 1785–1797, doi:10.1029/97JD02065.
- Skamarock, W. C., J. B. Klemp, J. Dudhia, D. O. Gill, D. M. Barker, W. Wang, and J. G. Powers, 2005: A description of the Advanced Research WRF version 2. NCAR Tech. Note NCAR/TN-468+STR, 88 pp., doi:10.5065/D6DZ069T.
- Smith, J. A., 1993: Marked point process models of raindrop-size distributions. J. Appl. Meteor., 32, 284–296, doi:10.1175/ 1520-0450(1993)032<0284:MPPMOR>2.0.CO;2.
- —, and W. F. Krajewski, 1993: A modeling study of rainfall ratereflectivity relationships. *Water Resour. Res.*, 29, 2505–2514, doi:10.1029/93WR00962.
- Srivastava, R. C., 1971: Size distribution of raindrops generated by their breakup and coalescence. *J. Atmos. Sci.*, **28**, 410–415, doi:10.1175/1520-0469(1971)028<0410:SDORGB>2.0.CO;2.
- Steiner, M., and J. A. Smith, 1998: Convective versus stratiform rainfall: An ice-microphysical and kinematic conceptual model. *Atmos. Res.*, 47–48, 317–326, doi:10.1016/ S0169-8095(97)00086-0.
- —, and —, 2000: Reflectivity, rain rate, and kinetic energy flux relationships based on raindrop spectra. *J. Appl. Meteor.*, **39**, 1923–1940, doi:10.1175/1520-0450(2000)039<1923: RRRAKE>2.0.CO;2.
- —, and —, 2004: Scale-dependence of radar rainfall rates—An assessment based on raindrop spectra. *J. Hydrometeor.*, **5**, 1171–1180, doi:10.1175/JHM-383.1.
- —, and R. Uijlenhoet, 2004: A microphysical interpretation of radar reflectivity-rain rate relationships. *J. Atmos. Sci.*, **61**, 1114–1131, doi:10.1175/1520-0469(2004)061<1114: AMIORR>2.0.CO;2.
- Sun, J., and N. A. Crook, 1997: Dynamical and microphysical retrieval from Doppler radar observations using a cloud model and its adjoint. Part I: Model development and simulated data experiments. *J. Atmos. Sci.*, **54**, 1642–1661, doi:10.1175/1520-0469(1997)054<1642:DAMRFD>2.0.CO;2.
- —, and —, 1998: Dynamical and microphysical retrieval from Doppler radar observations using a cloud model and its adjoint. Part II: Retrieval experiments of an observed Florida convective storm. *J. Atmos. Sci.*, 55, 835–852, doi:10.1175/ 1520-0469(1998)055<0835:DAMRFD>2.0.CO;2.
- —, and —, 2001: Real-time low-level wind and temperature analysis using single WSR-88D data. Wea. Forecasting, 16, 117– 132, doi:10.1175/1520-0434(2001)016<0117:RTLLWA>2.0.CO;2.
- —, M. Chen, and Y. Wang, 2010: A frequent-updating analysis system based on radar, surface, and mesoscale model data for the Beijing 2008 forecast demonstration project. *Wea. Forecasting*, 25, 1715–1735, doi:10.1175/2010WAF2222336.1.
- Testud, J., S. Oury, R. A. Black, P. Amayenc, and X. Dou, 2001: The concept of "normalized" distribution to describe raindrop spectra: A tool for cloud physics and cloud remote sensing. *J. Appl.*

- *Meteor.*, **40**, 1118–1140, doi:10.1175/1520-0450(2001)040<1118: TCONDT>2.0.CO:2.
- Thurai, M., W. A. Petersen, A. Tokay, C. Schultz, and P. Gatlin, 2011: Drop size distribution comparisons between PARSIVEL and 2-D video disdrometers. *Adv. Geosci.*, 30, 3–9, doi:10.5194/ adgeo-30-3-2011.
- Tokay, A., and D. A. Short, 1996: Evidence from tropical raindrop spectra of the origin of rain from stratiform versus convective clouds. *J. Appl. Meteor.*, **35**, 355–371, doi:10.1175/1520-0450(1996)035<0355: EFTRSO>2.0.CO;2.
- ——, W. A. Petersen, P. Gatlin, and M. Wingo, 2013: Comparison of raindrop size distribution measurements by collocated disdrometers. J. Atmos. Oceanic Technol., 30, 1672–1690, doi:10.1175/JTECH-D-12-00163.1.
- ——, D. B. Wolff, and W. A. Petersen, 2014: Evaluation of the new version of the laser-optical disdrometer, OTT Parsivel². J. Atmos. Oceanic Technol., 31, 1276–1288, doi:10.1175/ JTECH-D-13-00174.1.
- Uijlenhoet, R., J. A. Smith, and M. Steiner, 2003: The microphysical structure of extreme precipitation as inferred from ground-based raindrop spectra. *J. Atmos. Sci.*, **60**, 1220–1238, doi:10.1175/1520-0469(2003)60<1220:TMSOEP>2.0.CO;2.

- Ulbrich, C. W., 1983: Natural variations in the analytical form of the raindrop size distribution. *J. Climate Appl. Meteor.*, **22**, 1764–1775, doi:10.1175/1520-0450(1983)022<1764: NVITAF>2.0.CO:2.
- Vivekanandan, J., W. M. Adams, and V. N. Bringi, 1991: Rigorous approach to polarimetric radar modeling of hydrometeor distributions. J. Appl. Meteor., 30, 1053–1063, doi:10.1175/ 1520-0450(1991)030<1053:RATPRM>2.0.CO;2.
- Waldvogel, A., 1974: The N_0 jump of raindrop spectra. *J. Atmos. Sci.*, **31**, 1067–1078, doi:10.1175/1520-0469(1974)031<1067: TJORS>2.0.CO:2.
- —, W. Henrich, and W. Schmid, 1995: Raindrop size distributions and radar reflectivity profiles. Preprints, 27th Conf. on Radar Meteorology, Vail, CO, Amer. Meteor. Soc., 26–28.
- Webster, P. J., and R. Lukas, 1992: TOGA COARE: The Coupled Ocean–Atmosphere Response Experiment. *Bull. Amer. Meteor. Soc.*, **73**, 1377–1416, doi:10.1175/1520-0477(1992)073<1377: TCTCOR>2.0.CO;2.
- Yuter, S. E., D. E. Kingsmill, L. B. Nance, and M. Löffler-Mang, 2006: Observations of precipitation size and fall speed characteristics within coexisting rain and wet snow. J. Appl. Meteor. Climatol., 45, 1450–1464, doi:10.1175/JAM2406.1.